Continental collision with finite indenter strength: 2. European Eastern Alps

Jörg Robl and Kurt Stüwe

Institut für Erdwissenschaften, Universität Graz, Graz, Austria

Received 15 September 2004; revised 10 May 2005; accepted 6 June 2005; published 19 August 2005.

[1] Comparison of the results of a thin viscous sheet model with the velocity field determined by GPS stations in the Alpine-Pannonian realm shows that the Adriatic plate is only slightly stronger than the Eastern Alps. The observed velocity field is best approximated with a Newtonian fluid. However, this scenario must be fairly recent, as the overall geometry of the orogen can only be reproduced if the rheology contrast was about 1:10 before the late Miocene. The boundary conditions for this model are tested against the orientation of the intraplate stress field and are robust for Argand numbers between 1 and 5. We conclude that the convergence rate between the Adriatic and European plates must have slowed since the Miocene and that the present-day eastward extrusion of the Eastern Alps is largely due to lateral escape and only to a minor degree due to gravitational collapse. Scaled viscosities of the Eastern Alps are on the order of 10^{23} Pa s. **Citation:** Robl, J., and K. Stüwe (2005), Continental collision with finite indenter strength: 2. European Eastern Alps, *Tectonics*, *24*, TC4014, doi:10.1029/2004TC001741.

1. Introduction

[2] The eastern part of the European Alps has been described as a typical example of an orogen formed by indenting one continent into another. Within this model, the southern Adriatic plate is assumed to be rigid and is assumed to have indented obliquely into a softer region along the southern margin of the European plate [*Ratschbacher et al.*, 1991a, 1991b; *Frisch et al.*, 1998]. This model is consistent with the overall geometry of the Alps, with the region of maximum horizontal shortening being located north of the indenter front and long, orogen-parallel structures that fan out toward the east and extrude the orogen eastward toward the Pannonian Basin (Figure 1).

[3] However, several observations indicate that the Adriatic indenter cannot be assumed to be rigid in its present stage and, in fact, that there must be rheological variations within the European plate between the orogen and the European foreland in the far field. Field data also show that the indenter must have experienced significant changes in its rheology relative to the Eastern Alps over the past 30 m.y. For example, structural data from the Adriatic plate [e.g., *Castellarin and Cantelli*, 2000] and from the Eastern Alps [e.g., *Ratschbacher et al.*, 1991b] indicate that ever since the Eocene, the deformation was variably partitioned between the two colliding plates. While orogen parallel extension and lateral extrusion was the dominant feature during early to mid-Miocene times, the evolution of the orogen since the late Miocene was characterized by thrusting and surface uplift within the Adriatic plate [*Castellarin and Cantelli*, 2000; *Zattin et al.*, 2003]. Extrusion is also associated with some minor folding and even reverse faulting as evidenced by Miocene basins [e.g., *Nemes et al.*, 1997]. Today, most of the current seismicity is located within the Adriatic plate, while the region of largest crustal thickness inside the European plate is seismically comparatively calm (Figure 2a).

[4] Clearly, such observations show that the Adriatic plate cannot be assumed to be a rigid indenter throughout the evolution of the Alps and that not only changes in the kinematic boundary conditions play an important role in shaping the orogen, but that changes in the rheology must also be considered. In this study, we use observations on the partitioning of deformation between the European and the Adriatic plates to infer aspects of the rheology contrast between the two plates and its changes since the Miocene. In our approach, we use a two-dimensional numerical thin sheet model in plan view. In a companion paper we have introduced this numerical model and investigated the principles of deformation partitioning between two plates for indenters of finite strength [*Robl and Stüwe*, 2005]. In this paper, we apply a somewhat more refined model to the rheological evolution of the Adriatic-European collision zone. Details of our rheological assumptions and their justification are discussed in section 5. We show that the present-day stress, strain and velocity pattern of the Alpine orogen indicates that the Adriatic indenter has currently a rheology that is similar to that of the European plate, at least in the region of the orogen. However, we also show that the European plate must have been about an order of magnitude softer than the Adriatic plate in the Miocene.

[5] In our terminology we refer to the "Alpine orogen" as the general region of thickened crust and elevated topography on both the Adriatic and European plates. The term "Eastern Alps" is used for the region east of 9°30′E (the meridian of Lake Constance), corresponding to the western most exposure of typical units of the Eastern Alps. The Eastern Alps are therefore entirely located east

0278-7407/05/2004TC001741$12.00

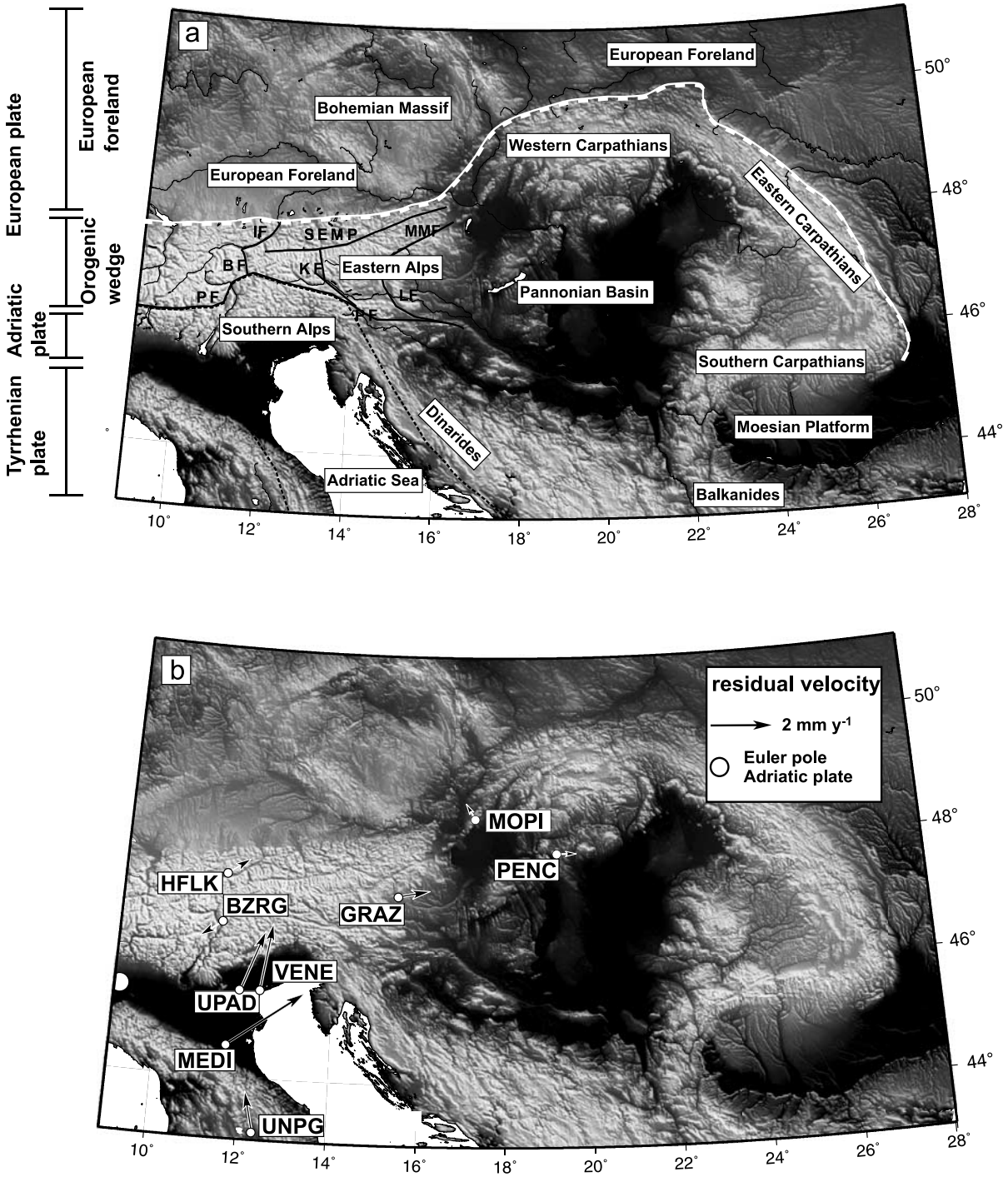

Figure 1. Topographic map of the investigated region showing (a) the most important geological units and structures discussed in the text and (b) the velocity field calculated from the motion of GPS station relative to the central European reference frame after *Nocquet and Calais* [2003]. The positions of the GPS stations are marked by circles. The topographic map is calculated from the SRTM30 digital elevation model and is shown in a transverse Mercator projection with a central meridian at 18°30′E. Major rivers are shown in Figure 1a for better orientation (thin black lines). Thick solid black lines indicate important faults within the Eastern Alps. PF, Periadriatic fault system; SEMP, Salzachtal-Ennstal-Maria Zell-Puchberg fault; KF, Katschberg fault; BF, Brenner fault; MMF, Mur-Mürz fault system; IF, Inntal fault; LF, Lavanttal fault. Dashed black lines show approximate position of plate boundaries. The thick white line indicates the position of the Alpine-Carpathian deformation front [modified after *Peresson and Decker*, 1997].

of the Euler pole of the Adriatic plate and lie therefore fully within a region of convergence between the two plates (Figure 1a) [*Nocquet and Calais*, 2003]. In the south the Eastern Alps are bound by the Periadriatic fault system that is explained in detail in section 2. We also use the term ''orogenic wedge'' for the Eastern Alps, as it appears to be a region of different rheology and kinematics to the remainder of the European plate. The European plate north of the Alpine orogen is referred to as the ''European foreland''. Note, that we use the term ''foreland'' here only for the far-field part of the European plate, while we use this term for the entire plate north of the indenter in our companion paper [*Robl and Stüwe*, 2005]. The ''Southern Alps'' is the part of the Alpine orogen that is located within the Adriatic plate. The Adriatic and European plates are separated by the Periadriatic fault system which has been described in some detail by *Mancktelow et al.* [2001].

[6] The terms related to lateral extrusion also need to be defined: ''Lateral extrusion'' refers to the general displacement of rocks parallel to the orogen that occurs in the Eastern Alps in response to the northward motion of the Adriatic plate [*Ratschbacher et al.*, 1989, 1991a]. The term was coined by *Ratschbacher et al.* [1991b] and encompasses the lateral displacement of rocks due to both ''tectonic escape'' and ''extensional collapse''. Both lateral motions form important components of the velocity field interpreted below, but they are caused by different stress fields. ''Tectonic escape'' describes the lateral motion of crustal blocks away from a zone of plate convergence in a compressional environment [*Tapponnier et al.*, 1982]. In the upper crust, tectonic escape will be accommodated by orogen-parallel strike-slip faults. ''Extensional collapse'' describes lateral displacement of rocks under horizontal deviatoric tension along lateral gradients of gravitational potential energy [*Dewey*, 1988; *Molnar and Lyon-Caen*, 1988; *Stüwe and Barr*, 2000]. Extensional collapse may be accommodated by normal faults oriented normal to the orogen. *England and Houseman* [1989] showed that the process of continental convergence may lead to tectonic escape, but can generally not lead to extensional collapse if the orogenic boundaries are constrained. Extensional collapse during continental convergence is only possible if the convergence rates or the rheological strength of the orogen decrease, or if other mechanisms can be invoked to insert additional potential energy into the orogen [*England and Houseman*, 1989; *Stüwe and Sandiford*, 1995]. It is in part the subject of this paper to evaluate the relative contribution of tectonic escape versus gravitational collapse in the lateral extrusion of the Eastern Alps.

2. Development of the Eastern Alps and Bordering Regions

[7] Our study focuses on aspects of the rheology of the Alps following the initial collision of the Adriatic and European plates. This was initiated with the final subduction of the last oceanic lithosphere of the Piemontais ocean in the Early Eocene [e.g., *Neubauer et al.*, 1999]. The subsequent continent-continent collision must be seen in view of the fact that on the European plate, the Austroalpine nappe stack was already a piece of overthickened crust from the earlier Eo-Alpine events [*Neubauer et al.*, 1999; *Liu et al.*, 2001]. During the collision, this nappe stack was partially overridden by the Adriatic plate. At the Early/Late Oligocene boundary around 30 Ma, crustal thickening in the European plate reached its maximum [*Frisch et al.*, 2000]. Thermal relaxation of this stack led to a zone of weak and easily deformable lithosphere between the stiff lower plate of the European foreland and the thermally weakened Adriatic upper plate [*Ratschbacher et al.*, 1991a; *Willingshofer and Cloetingh*, 2003]. This zone is what is here referred to as an orogenic wedge and coincides largely with the elevated region of the Eastern Alps (Figure 1a). Additional weakening of this wedge was caused by the rapid exhumation of hot material in the central orogenic wedge [*Genser et al.*, 1996; *Dunkl et al.*, 1998; *Kuhlemann et al.*, 2001] and by magmatic intrusions in the southern part of this wedge along the Periadriatic fault. These magmatic intrusions were caused by the slab break off of the subducted lithosphere [*von Blanckenburg and Davies*, 1995] and were accompanied by elevated heat flow in the wedge [*Sachsenhofer et al.*, 1997; *Sachsenhofer*, 2001; *Rosenberg*, 2004] and reduced lithospheric strength. The appearance of conglomerate fans within the Molasse basin north of the central and Eastern Alps indicates significant surface uplift at that time [*Frisch et al.*, 2000; *Kuhlemann and Kempf*, 2002].

[8] The early to middle Miocene evolution was dominated by the lateral extrusion of the Eastern Alps toward the east [*Ratschbacher et al.*, 1991a; *Frisch et al.*, 2000]. This was facilitated by the roll back of a subduction zone beneath the Carpathian arc [*Royden et al.*, 1983; *Cloetingh and Lankreijer*, 2001] causing large scale normal faulting and crustal thinning in the Pannonian domain. In the Eastern Alps, a corridor bordered by the dextral Periadriatic fault system (PF) in the south and by several large sinistral fault systems in the north (e.g., Salzachtal-Ennstal-Maria Zell-Puchberg (SEMP) fault) was affected by orogen parallel extension (Figure 1a) [*Peresson and Decker*, 1997]. Crustal blocks moved eastward between these strike slip zones and along large low-angle detachments like the Brenner and Katschberg normal faults [*Selverstone*, 1988; *Behrmann*, 1988; *Genser and Neubauer*, 1989; *Fügenschuh et al.*, 1997]. This period is characterized by the fast exhumation of core complexes [*Dunkl et al.*, 1998; *Dunkl and Demény*, 1997; *Kuhlemann et al.*, 2001] and the formation of intermontane basins [*Frisch et al.*, 1998, 2000].

[9] At the Badenian-Sarmatian boundary (around 13 Ma), the subduction beneath the Carpathian arc terminated. This led to an inversion of the stress field from extension to compression in the entire Eastern Alps–Pannonian realm [*Peresson and Decker*, 1997; *Cloetingh and Lankreijer*, 2001]. This inversion is indicated by buckling of the lithosphere in the Pannonian basin [*Horváth and Cloetingh*, 1996] and by recent stress data (J. Reinecker et al.,

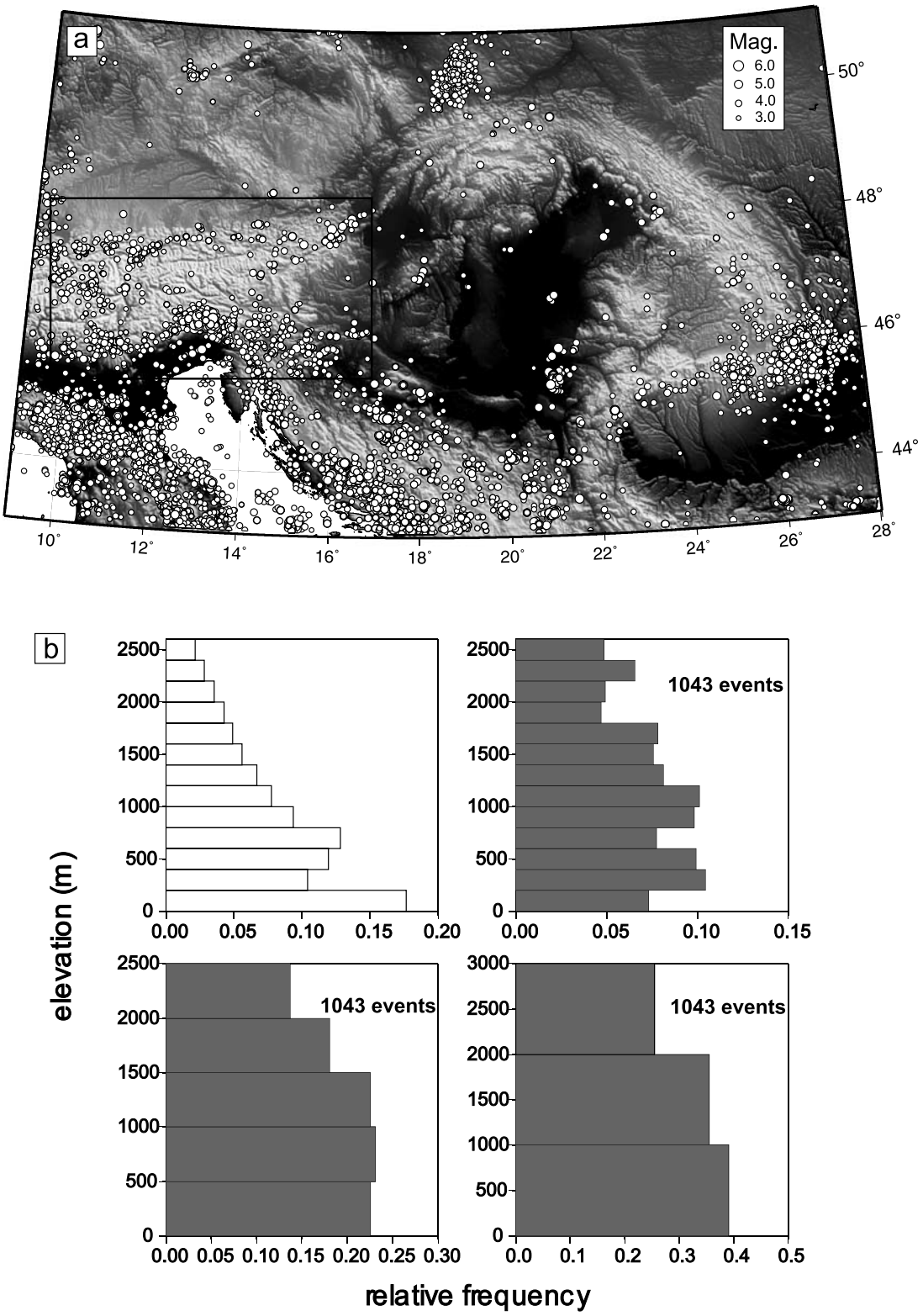
a
Mag.
6.0
5.0
4.0
3.0
50°
48°
46°
44°
10°
12°
14°
16°
18°
20°
22°
24°
26°
28°
b
elevation (m)
1043 events
1043 events
1043 events
relative frequency

Figure 2

2003 release of the World Stress Map, Res. Group of the Heidelberg Acad. of Sci. and Humanities, Heidelberg, Germany, available at www.world-stress-map.org). Because of the ongoing convergence between the counterclockwise rotating Adriatic plate and the European foreland, east directed lateral escape of crustal blocks is continuing with rates up to 4 mm yr^{-1} at the Alpine-Pannonian-Dinaric junction zone [*Grenerczy et al.*, 2000].

[10] As the Periadriatic fault separates the Adriatic indenter from the Eastern Alps, it represents a key feature in the evolution the whole domain. Its initial orientation and the amount of offset through its evolution are under debate. According to *Frisch et al.* [2000], this 700 km long fault system was originally oriented in an approximately east-west direction. Ongoing indentation of the Adriatic microplate led to the separation of the Periadriatic fault system into a western segment with sinistral displacement (the Guidicarie fault) and an eastern segment with dextral displacement (the Gailtal fault) [*Schmid et al.*, 1987, 1989; *Scarascia and Cassinis*, 1997]. However, according to *Viola et al.* [2001] this model is not supported by geochronological and structural data. Initial activation of the Guidicarie fault segment occurred before Miocene (in the Oligocene) and is therefore coeval with the other fault segments of the Periadriatic fault. The subsequent Miocene sinistral offset along the Guidicarie fault did not exceed 20 km. This implies that the initial geometry was comparable with the present-day situation [*Viola et al.*, 2001]. Whatever the case may be, the Periadriatic fault and other Miocene fault systems discussed above are not active today (compare Figure 1a and Figure 2a) and are therefore unlikely to control the velocity field interpreted here.

3. Present-Day Tectonic Setting

[11] The present-day dynamics of the Alpine-Pannonian realm (Figures 2 and 3) is predominantly the result of the Adriatic-European plate collision which is still evidenced by a high-velocity region in the upper mantle [*Lippitsch et al.*, 2003]. However, to be fully understood (in particular the stress field in the stable European foreland), the effect of the ridge push of the Mid Atlantic ridge must also be considered [*Gölke and Coblentz*, 1996]. A large number of stress data from the world stress map project (www.world-stress-map.org) allow the distinction of several stress provinces (Figure 3b). The European foreland is divided into a western and a central European stress province. The orientation of the maximum horizontal stress (σ_H) rotates gradually from north-west in the western part to north-east in the eastern part [*Gölke and Coblentz*, 1996; *Reinecker and Lenhardt*, 1999]. In general, the stress regime of the whole region is compressional (Figure 3a).

[12] The Bohemian massif shows a central European stress pattern with a northwest-southeast orientation of the maximum horizontal stress. This rigid block is surrounded by a radially oriented stress pattern indicating a high rheology contrast between the Bohemian massif and the surrounding regions [*Bada et al.*, 1998; *Reinecker and Lenhardt*, 1999]. The Adriatic stress province is characterized by a NNW-SSW oriented σ_H in the western part and ENE-WSE orientation of σ_H at the transition to the Dinaric stress province. The Eastern Alps represent the transition between the Adriatic and the western European stress province. Toward the Pannonian basin, the stress trajectories turn into an east-west orientation and diverge. The Adriatic realm is characterized by mainly reverse faulting. Fault activity within the Dinaric stress province shows both reverse and strike-slip faulting. Faults in the Eastern Alps and the Pannonian basin reflect a strike-slip stress regime.

[13] Because of the sparse distribution of GPS stations, the velocity field of the region is not as well constrained as the stress field. Nevertheless, it can be seen in Figure 1b that the direction and magnitudes of the velocities in the European plate are consistent with the stress field. The Adriatic plate is characterized by a north directed velocity of up to 2 mm yr^{-1} relative to the central European reference frame as measured in the GPS sites UPAD and VENE (Figure 1b) [*Nocquet and Calais*, 2003]. Toward the Pannonian basin, the velocity field rotates to the east. The velocity declines from west to east. An east directed velocity of about 1 mm yr^{-1} is measured at GRAZ and of about 0.6 mm yr^{-1} at PENC. Because of different calculation methods, increasingly longer time series and higher precision of GPS measurements, the calculated Euler pole and angular velocity of the Adriatic plate has changed significantly over the last 20 years from 45.8°N, 10.2°E [*Anderson and Jackson*, 1987] to 44.5°N, 9.5°E, 0.3° $m.y.^{-1}$ [*Westaway*, 1990] to 46.8°N, 6.3°E, 0.3° ± 0.06° $m.y.^{-1}$ [*Ward*, 1994] and finally to 45.36°N, 9.10°E, 0.52° $m.y.^{-1}$ [*Nocquet and Calais*, 2003].

[14] Active deformation of the Adria-Europe collision zone is also demonstrated by high seismicity in the region. Figure 2a shows that both the Adriatic plate and the European plate are seismically active, with a total of 1043 seismic events above magnitude 3, collected by the Incorporated Research Institutions for Seismology (IRIS) database (http://www.iris.edu/) since 1960, within the box shown in Figure 2a. Interestingly, Figure 2b shows that

Figure 2. Distribution of seismicity in the Alpine-Pannonian realm. Seismic events are taken from the Incorporated Research Institutions for Seismology (IRIS) data set (www.iris.edu). (a) Map showing 7805 seismic events with magnitudes between 3 and 6.4 from the time span between 1960 and 2004. The size of the circles is proportional to the magnitudes of the seismic events (see legend). The box indicates the region for which the seismic events are plotted in Figure 2b. (b) Distribution of earthquakes (in the boxed region of Figure 2a) with elevation, normalized to 1. The top left plot shows the distribution of elevation within this region; 3% of the region is above 2500 m elevation, and about 10% of the region is between 250 and 500 m elevation. The top right, bottom left, and bottom right plots show the distribution of earthquakes with elevation, where elevation is sliced into slabs of 200, 500, and 1000 m thickness, respectively.

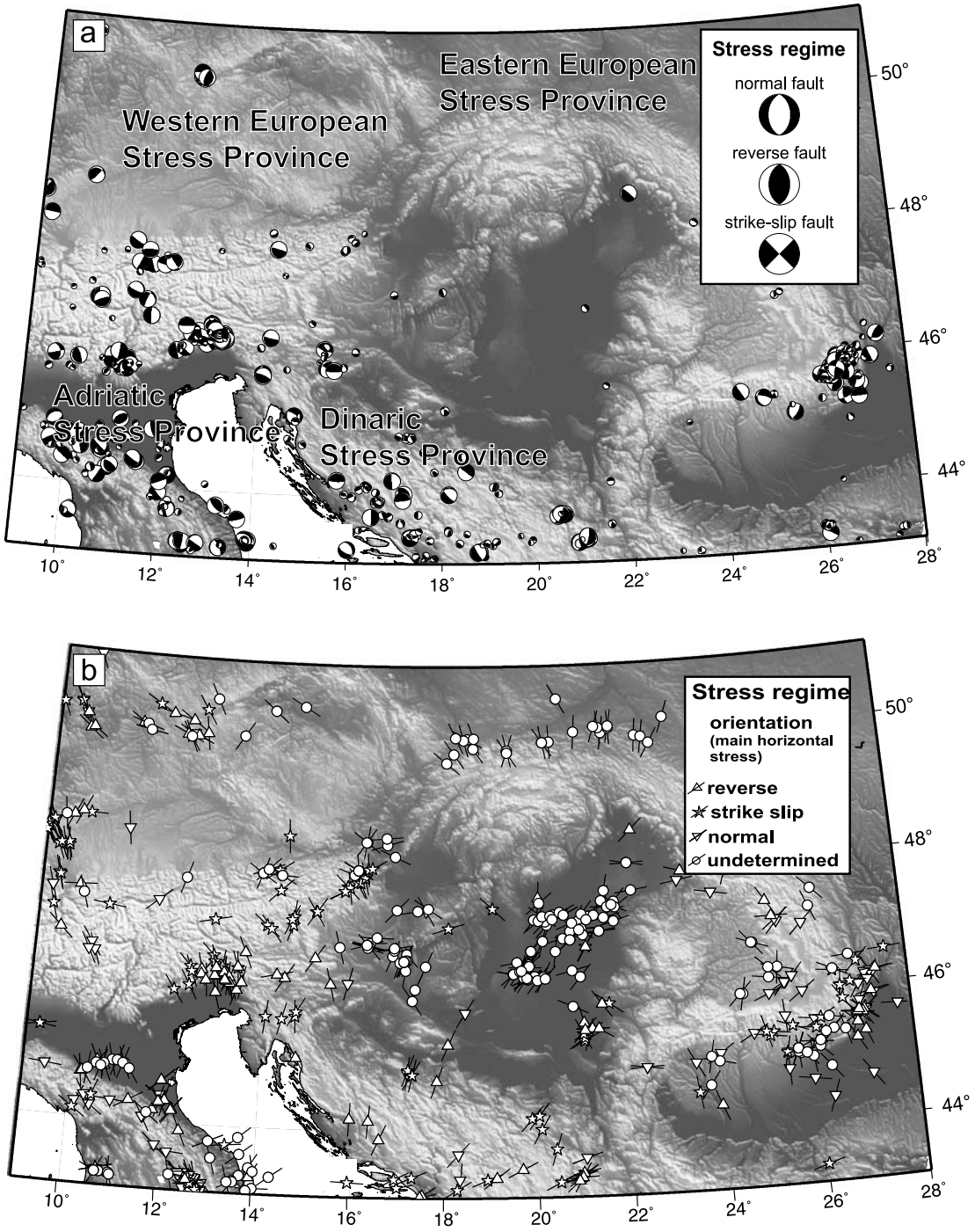

Figure 3. Data constraining the present-day tectonic setting of the study region. (a) Stress regime, orientation, and magnitude of seismic events as constrained by seismic focal mechanisms (A. O. Mostrioukov and V. A. Petrov, Catalogue of Focal Mechanisms of Earthquakes 1964–1990, 1994, available at http://www.brk.adm.yar.ru/). The symbol size of the focal mechanisms is proportional to the seismic moment. (b) Orientation and qualitative nature of the intraplate stress field from the World Stress Map project (www.world-stress-map.org).

there is a correlation between surface elevation and seismicity: the Eastern Alps are surrounded by regions of high seismicity while the topographically highest region appears seismically comparatively calm. This relationship is highlighted by plotting the number of seismic events against the surface elevation above the epicenter (Figure 2b). It may be seen, that about twice as many seismic events occur per area at surface elevations below 1000 m than occur per area above 2000 m. While this may be related to the simple fact that the topographically low valleys in the Eastern Alps are incised along faults, it also may indicate that deformation of the orogen has propagated to the foothills, while the regions of high potential energy regions are seismically calm.

4. Model

[15] In order to extract rheological information on the Europe-Adria collision zone from the stress and velocity data discussed above, we employ a two-dimensional thin sheet model of the region shown in Figures 1, 2, and 3. While a thin sheet model represents a gross simplification of the three-dimensional geometry of the orogen (e.g., compare horizontal length scale of the orogen to its depth extent as shown by tomography [*Lippitsch et al.*, 2003]), our model describes a two-dimensional end-member of the mechanics of this mountain belt. Together with other two-dimensional models that have been published on cross sections [*Willingshofer et al.*, 1999; *Pfiffner et al.*, 2000] our plan view model completes a series of two-dimensional numerical models that have, albeit separately, considered all three spatial dimensions of the orogen.

[16] Because our model is two-dimensional, it is necessary to average vertical rheological variations in the crust. Although we will test our model against velocities measured on the surface of the brittle crust, at least two thirds of the crust are likely to behave viscously [e.g., *Sonder and England*, 1986]. We therefore chose to model a viscous rheology. We consider both linear and nonlinear viscous rheologies and explore the dependence of our results on changes in the nonlinearity as expressed in the power law exponent n. This is of interest because highly nonlinear viscous rheologies will cause localization of strain in regions of stress gradients and will therefore begin to approximate brittle plastic behavior.

[17] In order to solve the force balance equations in two dimensions for the assumed rheology, we have used the finite element code BASIL of *Barr and Houseman* [1996], which is explained in detail in our companion paper [*Robl and Stüwe*, 2005]. The code has also been used successfully to describe other orogens, in particular the India-Asia collision zone [*England and Houseman*, 1986, 1989; *Houseman and England*, 1986]. However, in contrast to previous applications of this model, we have considered the evolution of the Alpine orogen too complex to justify a time-dependent exploration of the collision process. Instead, we model only the incremental deformation of the orogen at the present time and make some rough extrapolations to the past, so that we can infer the rheological changes since the Miocene. Nevertheless, in order to apply the finite element code to describe the Alps, we have performed several adaptations of the code.

[18] First, a routine was implemented that allows to preallocate a crustal thickness to every grid node, so that the instantaneous deformation field of the orogen can be calculated on the basis of an existing distribution of the potential energy (L. Evans, personal communication, 2003). For this we assume that the crustal thickness S is directly related to topography E, that topography is fully isostatically compensated and that crustal thickness variations are the only contribution to gravitational potential energy (Figure 4). Then, the relationship between crustal thickness and surface elevation can be described by

$$S = S_0 + (E - E_0)\Delta\rho, \tag{1}$$

where $\Delta\rho$ is the density contrast between crust (ρ_c) and mantle (ρ_m) and is given by $\Delta\rho = \rho_m/(\rho_m - \rho_c)$. The densities are assumed to be $\rho_m = 3100$ k gm^{-3} and $\rho_c = 2700$ k gm^{-3}. E_0 and S_0 are the default surface elevation and crustal thickness for which we assume $E_0 = 100$ m and $S_0 = 35$ km, respectively. The density contrast and the default values for surface elevation and crustal thickness are chosen, so that doubling the crustal thickness corresponds to an elevation of about 4600 m. Although we have introduced these variables for crustal thickness and surface elevation, it is important to note that our model is not three-dimensional but a thin sheet model. Thus all lithospheric thickness parameters are only implemented in terms of a dimensionless layer thickness L' that is given by $L' = L/D$, where L is the real layer thickness and D is the horizontal length scale. The default value for L is set to $L_0 = 100$ km and D is set to one radian of the Earth as detailed below. By introducing topography, the original layer thickness is perturbed. The dimensionless layer thickness can be expressed in terms of crustal thickness or surface elevation:

$$L' - L'_0 = \left(\frac{(S - S_0) \times L_0}{D \times S_0}\right) = \left(\frac{(E - E_0) \times \Delta\rho \times L_0}{D \times S_0}\right). \tag{2}$$

The dimensionless layer thickness is derived from equation (2) and using a digital elevation model to define E. Nevertheless, all results presented below are scaled using Table 1 to convert dimensionless values to real values (see Appendix A).

[19] As a second adaptation, the finite element code of *Barr and Houseman* [1996] was adapted to perform thin viscous sheet calculations in spherical coordinates. This adaptation was performed by G. Houseman (personal communication, 2003) and is used here for the first time. Our model region spans 19° in longitude, which corresponds to roughly 0.4 radian. While this implies that curvature may play only a minor role over the arc length of the study region, it is important to note that it determines our choice of horizontal length scale as 1 radian or about $D = 6378$ km.

[20] Finally, we generalized the model by implementing a facility that allows the insertion of regions of general shape and variable rheology into the finite element mesh. Trian-

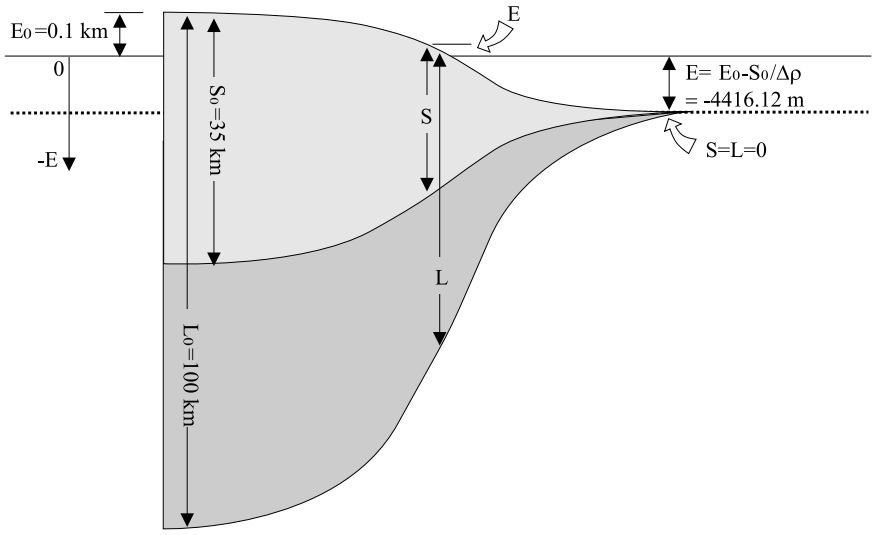

Figure 4. Cartoon illustrating the relationship between surface elevation (E), crustal thickness (S), and layer thickness (L) in the thin viscous sheet model used here. E_0, S_0, and L_0 are the default values for elevation, crustal thickness, and layer thickness. Note that the actual calculations are performed in terms of dimensionless layer thickness (see equation (2) in text).

gulation of meshes was previously used in BASIL to produce meshes around simple geometrical regions of variable rheology by using the computer program "polycircle" by L. Evans (personal communication, 2001) and a robust mesh generator [*Shewchuck*, 2002]. This was used, for example, by *Tenczer et al.* [2001] or *Biermeier et al.* [2001]. For further generalization, a program called "TraceIt" was written for the present study. The program reads several formats of map images in Mercator projection and enables the user to create a list of vertices with a few mouse clicks (for details see Appendix B). Results of TraceIt can be directly read by BASIL to create a general mesh that contains all node points chosen by the user.

5. Initial and Boundary Conditions

[21] For our model calculations we apply horizontal boundary conditions to the region shown in Figure 5 and define variable layer thickness and rheology contrasts inside the model region. The northern, western and eastern boundaries of the modeled region are those also shown in Figures 1 and 2. The boundaries in the north and east are located well within the European foreland. This region shows low seismicity and little internal deformation (Figures 1 and 2), so that we apply zero velocity normal and tangential to this boundary. The southern boundary is of interest here and is discussed in detail below. The western boundary is the most problematic one, as it must run somewhere through the orogen unless the entire central European realm is modeled, which we tried to avoid. Here we chose a western boundary of the model region which runs through the Euler pole of the Adriatic plate at about 9°E. North of the Euler pole the north-south velocity of the Adriatic plate must be zero and, because the Euler pole is located near the northern boundary of the plate, there is no significant east-west directed velocity related to plate rotation either. This is partly confirmed by GPS studies that show significant west and south directed velocities in the Western Alps, but north and east directed velocities in the Eastern Alps and Pannonian realm [*Nocquet and Calais*, 2003], suggesting some symmetry about the Euler pole. To minimize boundary effects, zero stress is set in tangential direction along the western boundary. In the European foreland sector of the western boundary the tangential boundary condition is of little importance, as the modeled north-south velocities in this region are practically zero.

[22] The southern boundary of the maps shown in Figures 1 and 2 is located well within the Tyrrhenian plate and contains regions of extremely high seismicity in the Appenines, which is outside our region of interest. Thus we chose to model only the region north of the 45th parallel. North of this line the Po plain is largely aseismic. Along this boundary we apply zero velocity in tangential direction and zero stress in normal direction, except in a boundary segment west of 15°E which is occupied by the counterclockwise rotating Adriatic plate. This segment is described

Table 1. Scaling of Dimensionless Values Used in BASIL to Actual Values[a]

Variable	Model Value	Dimension	Actual Value
Length	x', y'	D	x, y
Velocity	u'	U_0	U
Time	t'	D/U_0	t
Strain rate	$\dot{\varepsilon}'$	U_0/D	$\dot{\varepsilon}$
Viscosity	η'	$B/2$	η
Stress	σ'	η/t	σ

[a]Model value times dimension equals actual value.

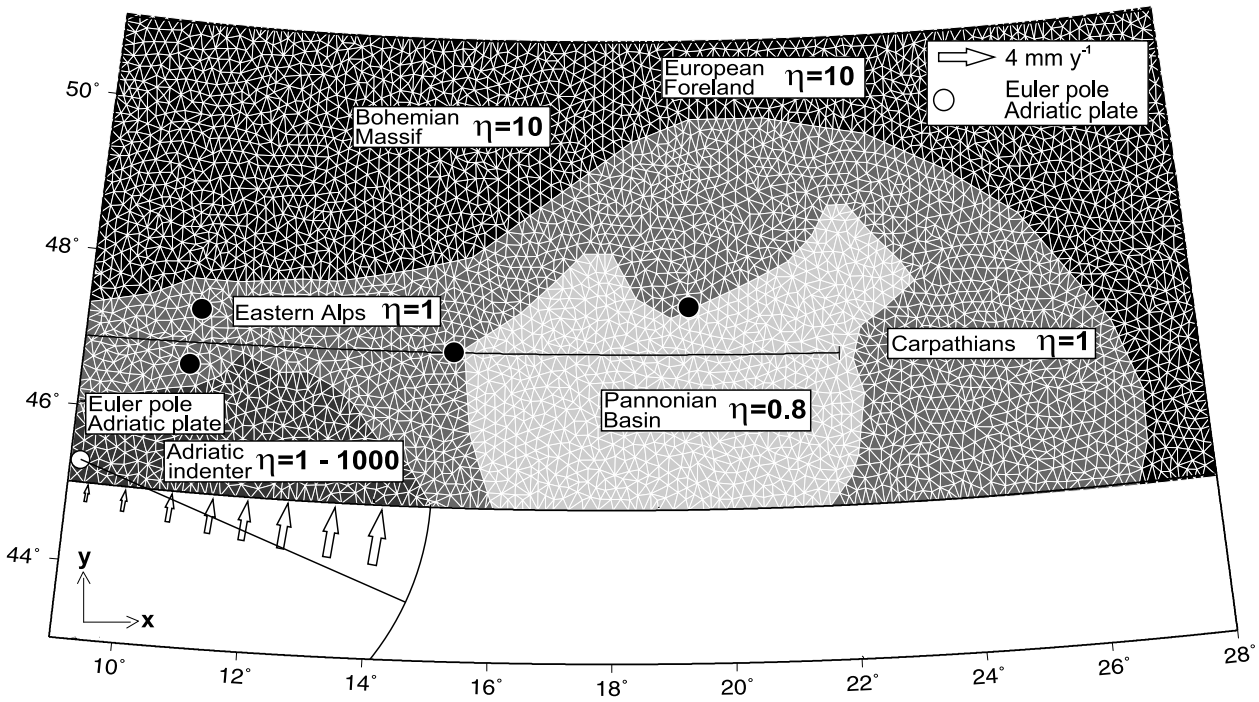

Figure 5. Model setup and boundary conditions. The shading shows four different zones of different rheology as indicated. The white circle shows the position of the Adriatic Euler pole. White arrows indicate the direction and magnitude of the velocity applied to the model boundary. The black line at 47°N from 9°E and 22°E shows the position of velocity profiles shown in Figure 7. The four black dots are, from west to east, the locations of the GPS stations BZRG, HFLK, GRAZ, and PENC (see also Figure 1b), for which velocities are discussed in Figures 7 and 8.

by an increasing north directed velocity from west to east, according to an Euler pole of the Adriatic plate at 45.36°N, 9.10°E and a counterclockwise angular velocity of 0.52° m.y.$^{-1}$ [*Nocquet and Calais*, 2003]. Taking this Euler pole and angular velocity, the maximum north directed velocity of 4 mm yr^{-1} occurs at the eastern end of the indenter and decreases to the west. The east directed component of the velocity vector is constant at 0.4 mm yr^{-1} over the whole indenting boundary (Figure 5).

[23] Inside the model region, a potential energy function was predefined by interpolating a digital elevation model onto the finite element mesh. We used the SRTM30 data set [*Farr and Kobrick*, 2000] with a Gaussian filter and a filter wavelength of 50 km to eliminate features of wavelengths that are substantially shorter than the elastic thickness of the lithosphere. The filtered data are then resampled at every 5 arc min, so that resolution of our digital elevation model is comparable to that of the finite element mesh. Filtering and resampling was performed with GMT3.4.3 [*Wessel and Smith*, 1991]. Filtered and resampled elevation data are used to calculate a dimensionless layer thickness with equation (2) at every grid node of the finite element mesh using a bilinear interpolation routine.

[24] Four zones of different rheology are defined inside the model region: the European foreland, the Pannonian basin, the Adriatic plate and the Eastern Alps. The boundaries of these four regions were chosen to follow the plate boundaries shown in Figure 1a, and lines of high heat flow contrast. The European foreland including the Bohemian massif is known as a rigid block. This is indicated by the low seismicity, negligible residual velocities [*Nocquet and Calais*, 2003] and the radial stress pattern around the south Bohemian spur [*Reinecker and Lenhardt*, 1999; *Bada et al.*, 1998]. Thus the European foreland north of the Alpine-Carpathian deformation front (Figure 1a) is set to be hard enough so that the modeled strain rates are negligible. This is about 10 times as viscous as the Eastern Alps. The crust of the Pannonian basin is thin compared to the crust in the Eastern Alps and weakened by the elevated average heat flow (90 mW m^{-2}) [*Bada et al.*, 1999]. It is therefore likely to be softer than the orogen. The effective viscosity of this region is set to 0.8 times the viscosity of the Eastern Alps. Substantially higher or lower viscosity contrasts will both cause a decrease in the modeled velocities inside this region that are lower than those observed (Figure 1b). The viscosity contrast (η) of the Adriatic plate with the Eastern Alps is of interest here and is used as a variable in the model calculations. In our model runs we vary this viscosity contrast, from $\eta = 1$ to $\eta = 1000$ (Figure 5).

6. Model Results

[25] In order to find an adequate rheology model for the Eastern Alps and the surrounding domains, we have com-

pared numerical models for a wide range of different rheologies with field data. In particular, we explore the influence of the Argand number (*Ar*), the non linearity of the viscosity (n) and the viscosity contrast (η) on the velocity and stress field. A detailed description of these parameters is presented in the companion paper [*Robl and Stüwe*, 2005]. The present-day stress and velocity fields are compared with incremental time step calculations of our model.

6.1. Stress Field

[26] The orientation of the axis of maximum compressional horizontal stress (σ_H) is sensitive to the applied boundary conditions. It provides therefore a good test to control the model geometry and its boundary conditions. Figure 6 shows that there is a good coincidence between modeled and measured orientation of the σ_H of the major stress provinces as discussed in the literature [e.g., *Reinecker and Lenhardt*, 1999]. Measured stress data often reflect only a local state of stress (see www.world-stress-map.org), so that smoothing and extrapolation algorithms [e.g., *Hansen and Mount*, 1990] are used to determine a consistent stress pattern [e.g., *Bada et al.*, 1998]. Deviations between the modeled and smoothed stress field in the European foreland are caused by the complex origin of σ_H. The stress field of the investigated region is a result of the ridge push along the Mid-Atlantic ridge and of collisional forces along the southern and eastern plate boundaries [*Gölke and Coblentz*, 1996]. As our interest here focuses on the processes along the southern boundary of the model region we have neglected forces acting on the western and eastern plate boundaries, which cause the differences between the modeled and the measured stress field in the European foreland as shown in Figure 6. Nevertheless, in the Eastern Alps and the Pannonian region, modeled and smoothed stress data coincide well and we therefore suggest that the boundary conditions discussed above are appropriate to describe the collision geometry.

[27] Although the orientation of the modeled stress field is sensitive to the applied boundary conditions, it is robust with regard to the internal rheology. For example, the orientation of the maximum horizontal stress is almost identical in Figures 6a and 6b, although the rheology contrast between the Adriatic plate and the Eastern Alps is 10 times larger in Figure 6b. In contrast to its orientation, the magnitude of the modeled stress field is sensitive to the internal rheology, but stress magnitudes are not very well constrained by field data. Thus we use the modeled velocity field and compare it to the relative velocities between the region of interest and the central European reference frame (residual velocities) as constrained by GPS data in the remainder of our considerations.

6.2. Velocity Field

[28] In order to compare the GPS-determined velocity field with the modeled velocity field, we begin by comparing velocities along an east-west profile at 47°N from 9°E to 22°E. This line is shown in Figure 5 and transects the entire Eastern Alps from west of the Tauern Window to east of the Pannonian basin. This profile includes many of the features known to be characteristic for the lateral extrusion of the Eastern Alps during the Miocene [*Ratschbacher et al.*, 1991a] and still shows evidence for substantial east directed residual velocities [*Nocquet and Calais*, 2003]. A more general comparison with several GPS stations is also shown in Table 2.

[29] Profiles for east and north directed components of the velocity vectors (u_x and u_y) are shown in Figure 7. Velocity profiles are presented for a Newtonian rheology ($n = 1$) and a highly nonlinear rheology ($n = 3$), for two different Argand numbers and for two viscosity contrasts between the Adriatic plate and the Eastern Alps of $\eta = 3$ and $\eta = 10$. Overall it may be seen that the Argand number has a small influence on the velocity field and that an increasing power law exponent leads to smoother changes in the velocity from west to east. Maxima and minima are also shifted because of the stronger strain localization with increasing n.

[30] For $\eta = 3$, u_x shows slight west directed motion in the western part of the profile (Figure 7a). At 13°E a rapid inversion to east directed motion occurs. The eastward velocity reaches a maximum at around 15°E. Further eastward, u_x decreases rapidly for $n = 1$ and smoothly for $n = 3$. At the eastern end point of the profile, $u_x \approx 0$ mm yr^{-1} for $n = 3$, while there is still significant east directed motion for $n = 1$. The culmination point for u_y at about 13°E is caused by the increasing northward motion of the Adriatic plate from east to west and by the triangular shape of the indenter (Figure 7b). The maximum u_y for $n = 1$ is about 50% larger than for $n = 3$. From the peak, u_y decreases rapidly to around zero at the eastern end of the profile. For $\eta = 10$ the shape of the profiles is similar but differs in some points. The profiles for u_x show pronounced west directed motion from 13°E westward and reach with about 1 mm yr^{-1} higher values than the maximum west directed velocity for the same model run for $\eta = 3$ (compare Figures 7a and 7c). Peak values for u_y larger than 2 mm yr^{-1} are reached for $\eta = 10$ (Figure 7d). This is clearly related to the high viscosity contrast of the indenter, which transmits most of the velocity applied on the boundaries to the Eastern Alps. To summarize the results explored in Figure 7, an increasing viscosity contrast leads to increasing west directed velocities in the western part of the profile and an overall increasing northward motion. A smoother shape of the velocity profiles and lower peak values of u_x and u_y occur for increasing n. The magnitude of *Ar* is only of secondary importance.

[31] Although Figure 7 is useful to illustrate the modeled changes in the velocity field from east to west, it is difficult to use for the comparison of modeled and measured velocities. This is (1) because it does not consider velocities in the Adriatic plate and (2) because it is difficult to explore the entire parameter space of η and n in Figure 7. In order to generalize our results and to investigate the influence of n and η on the velocity field, we therefore compare the modeled velocity with measured velocities at

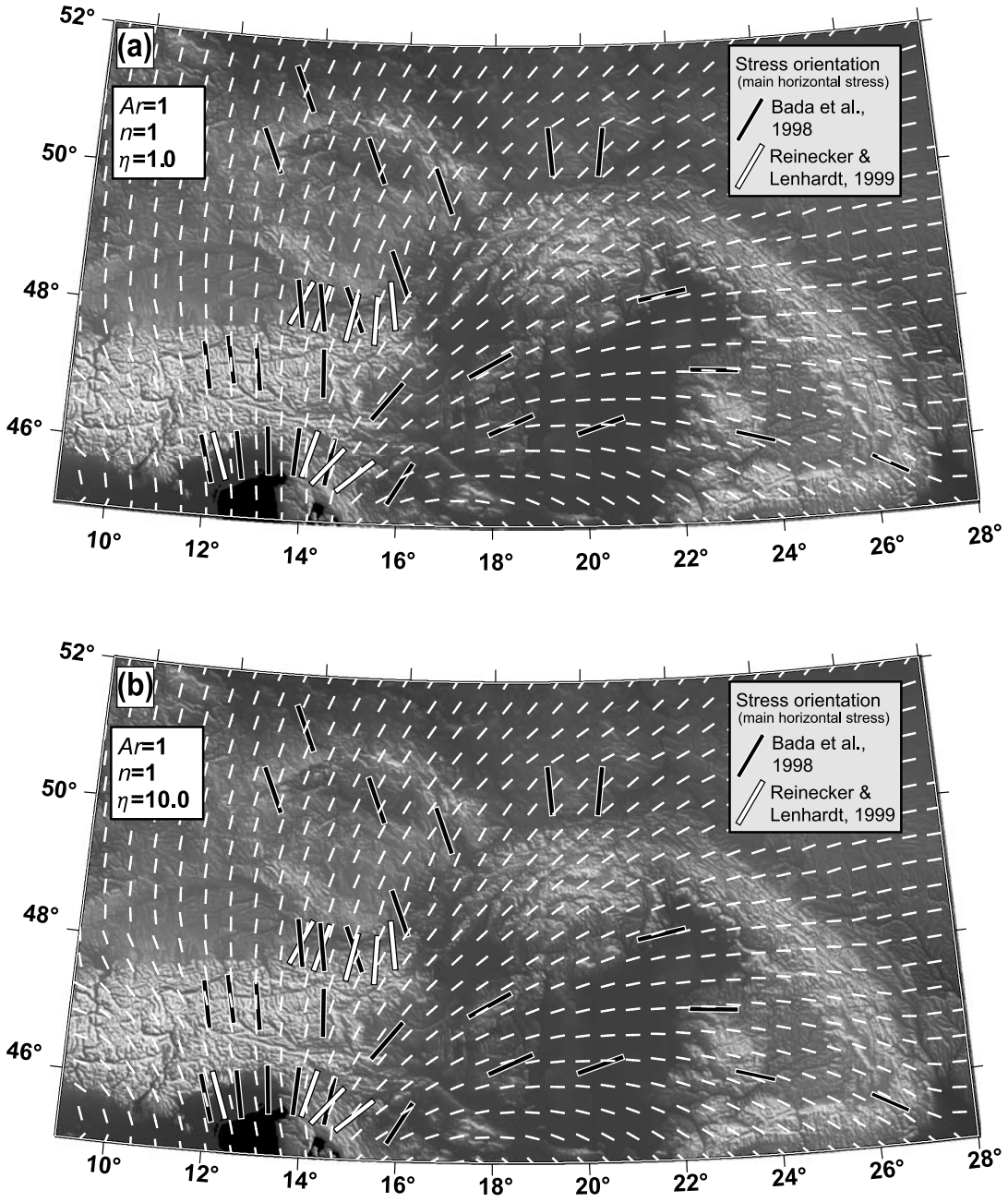

Figure 6. Comparison of the measured and modeled orientation of the maximum horizontal stress field (σ_H) for two different rheology contrasts between the Adriatic plate and the Eastern Alps of (a) $\eta = 1$ and (b) $\eta = 10$. The thin white dashes show the orientation of the modeled stress field. The thick bars indicate the orientation of the measured intraplate stress field as smoothed from the data of the World Stress Map project by *Bada et al.* [1998] and *Reinecker and Lenhardt* [1999] as indicated in the legend. Note that the orientation of the modeled stresses is quite robust toward the rheology contrast so that there is little difference between Figures 6a and 6b.

selected GPS stations in Figure 8. Figure 8 shows modeled horizontal velocity contours in the coordinate system n versus η at three geographic locations: The location of the GPS stations VENE (in the Adriatic domain), GRAZ (in the Eastern Alps) and PENC (in the Pannonian basin) (see Figure 1 for the location of the GPS stations). These stations were chosen because they show significant residual velocities relative to the central European reference frame, with standard deviations that are relatively small compared to the magnitude of motion (see also Table 2). It may be

Table 2. Comparison of Modeled and Measured Velocities for a Series of GPS Stations in the Alpine-Pannonian Realm[a]

	Measured Values				Modeled Values							
					Ar = 1				*Ar* = 3			
Station	Long	Lat	Velocity	GPS	η = 1	η = 3	η = 10	η = 100	η = 1	η = 3	η = 10	η = 100
					Power Law Exponent n = 1							
UPAD	11.88	45.41	u_x	0.7 ± 0.1	0.15	0.14	0.08	0.01	0.20	0.17	0.09	0.02
			u_y	2.0 ± 0.1	(2.04)	2.17	2.26	2.31	(2.00)	2.16	2.25	2.31
VENE	12.33	45.44	u_x	0.3 ± 0.2	(0.18)	(0.16)	0.08	−0.01	(0.23)	(0.18)	0.09	−0.01
			u_y	2.2 ± 0.3	(2.34)	(2.49)	2.60	2.66	(2.30)	(2.48)	2.59	2.66
GRAZ	15.49	47.07	u_x	1.0 ± 0.1	0.83	(0.87)	0.75	0.59	(0.99)	(1.02)	0.88	0.70
			u_y	0.2 ± 0.1	0.71	1.04	1.32	1.56	0.63	0.96	1.26	1.51
PENC	19.28	47.79	u_x	0.6 ± 0.2	(0.40)	(0.49)	(0.52)	(0.54)	(0.44)	(0.51)	(0.55)	(0.57)
			u_y	0.0 ± 0.2	(0.05)	(0.09)	(0.13)	(0.17)	(−0.05)	(−0.01)	(0.03)	(0.08)
BZRG	11.34	46.50	u_x	−0.7 ± 0.6	−0.06	(−0.29)	(−0.67)	(−1.04)	0.03	(−0.23)	(−0.64)	(−1.04)
			u_y	−0.5 ± 0.7	1.05	1.47	1.76	1.91	0.99	1.45	1.75	1.91
HFLK	11.39	47.31	u_x	0.7 ± 0.1	−0.01	−0.28	−0.70	−1.17	0.06	−0.22	−0.66	−1.15
			u_y	0.5 ± 0.2	(0.66)	1.07	1.42	1.65	(0.69)	1.11	1.47	1.71
MOPI	17.27	48.37	u_x	−0.3 ± 0.3	0.41	0.51	0.55	0.57	0.46	0.56	0.60	0.61
			u_y	0.5 ± 0.4	(0.23)	(0.32)	(0.39)	(0.46)	(0.19)	(0.28)	(0.35)	(0.42)
					Power Law Exponent n = 3							
UPAD	11.88	45.41	u_x	0.7 ± 0.1	0.09	0.11	0.10	0.04	0.11	0.12	0.11	0.04
			u_y	2.0 ± 0.1	1.89	(2.02)	2.14	2.26	1.83	(1.98)	2.12	2.25
VENE	12.33	45.44	u_x	0.3 ± 0.2	0.09	(0.12)	(0.11)	0.03	(0.11)	(0.13)	(0.13)	0.04
			u_y	2.2 ± 0.3	(2.11)	(2.27)	(2.42)	2.59	(2.05)	(2.23)	(2.40)	2.59
GRAZ	15.49	47.07	u_x	1.0 ± 0.1	0.21	0.30	0.35	0.30	0.23	0.34	0.39	0.34
			u_y	0.2 ± 0.1	(0.15)	(0.28)	0.41	0.59	(0.14)	(0.27)	0.41	0.58
PENC	19.28	47.79	u_x	0.6 ± 0.2	0.05	0.08	0.10	0.10	0.05	0.08	0.11	0.11
			u_y	0.0 ± 0.2	−0.01	0.00	0.00	0.02	−0.01	−0.01	−0.01	0.01
BZRG	11.34	46.50	u_x	−0.7 ± 0.6	−0.05	(−0.13)	(−0.31)	(−0.80)	−0.02	−0.08	(−0.27)	(−0.77)
			u_y	−0.5 ± 0.7	0.76	1.11	1.45	1.80	0.70	1.06	1.42	1.79
HFLK	11.39	47.31	u_x	0.7 ± 0.1	0.00	−0.08	−0.26	−0.75	0.02	−0.05	−0.24	−0.73
			u_y	0.5 ± 0.2	(0.40)	(0.68)	0.98	1.33	(0.40)	(0.69)	1.01	1.38
MOPI	17.27	48.37	u_x	−0.3 ± 0.3	0.07	0.10	0.13	0.14	0.07	0.12	0.15	0.16
			u_y	0.5 ± 0.4	0.02	0.04	0.07	(0.10)	0.02	0.04	0.07	(0.10)

[a]Station names are the international abbreviations for the GPS stations, and their location is shown in Figure 1b. Long means longitude; Lat means latitude. Measured velocities are from *Nocquet and Calais* [2003]. Modeled velocities that are within the standard deviation of the measured data are given in parentheses. The measured data shown for stations VENE, GRAZ, and PENC are those also shown in Figure 8 where a larger model parameter space is explored.

seen that the modeled velocities at the chosen three locations are generally larger for low n and high η (Figure 8) and are strongly dependent on the power law exponent n. It may also be seen that modeled and measured velocities match most GPS stations for low rheology contrasts below about η = 3 and low power law exponents around n = 1 (white dot in Figure 8). It is concluded that these values for the rheological parameters provide a good model to reproduce the velocity field in the Alpine-Pannonian realm.

[32] The good match between modeled and measured velocities for n = 1 and η < 3 for the stations shown in Figure 7 is also illustrated in Table 2. Other stations shown in Table 2 can only partly be compared with the model results: UPAD and HFLK show good matches for u_y for low η but no match for u_x for any *Ar*, η or n, so that their measured velocities are likely to relate to causes not explored here. In fact, station HFLK is known to be subject to significant seasonal changes in position (P. Pesec, personal communication, 2003) and station UPAD is located within a seismically active zone so that its velocity may be related to local causes. The measured velocities at stations MOPI and BZRG have standard deviations of about 100% and their correlation with the modeled data is therefore arbitrary.

[33] To illustrate the good match between modeled and measured velocity field for η < 3 and n = 1 across the entire study region, Figures 9a and 9b show the horizontal velocities in the model region for η = 1.5, n = 1 and *Ar* = 1. The choice of this Argand number implies a viscosity of 1.3×10^{23} Pa s for the Eastern Alps and 2.0×10^{23} Pa s for the Adriatic plate, but it was shown above that the velocity is not very sensitive to Argand number (and therefore absolute viscosity, see Table 1). The orientation of the velocity field shows the same pattern as the stress field in Figure 6. The modeled total magnitude of velocity fits very well with the measured total motion at various GPS locations, in particular at UPAD, VENE and PENC (Figure 9a and Table 2). For GRAZ only the eastward component of the velocity fits the measured data for u_x well (Figure 9b),

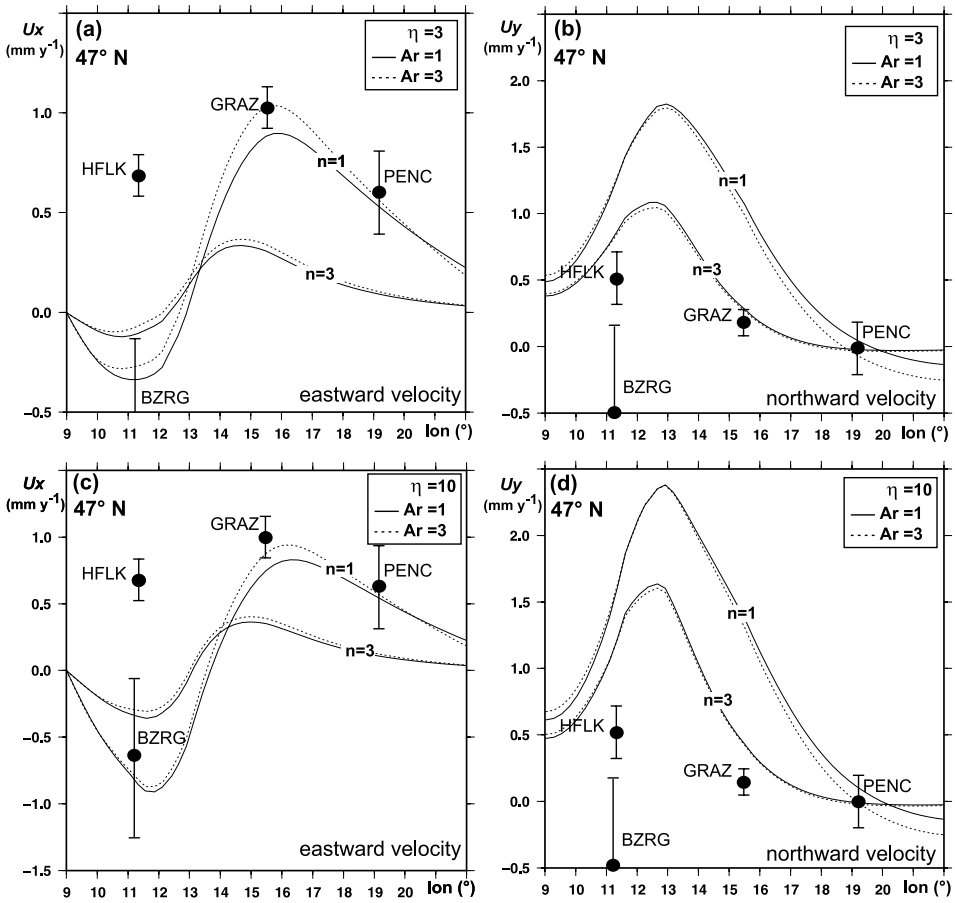

Figure 7. Modeled velocity profiles along the profile shown as the black line in Figure 5. Solid curves indicate model runs with $Ar = 1$. Dashed curves are for $Ar = 3$. Curves are shown for two different power law exponents ($n = 1$ and $n = 3$). (a and b) East-north directed components of the velocity (u_x and u_y) for a viscosity contrast $\eta = 3$. (c and d) East and north directed velocity components for a viscosity contrast $\eta = 10$. Measured residual velocities with error bars from four selected GPS stations near the profile line are shown for comparison. For more detail, see Figure 8 and Table 2.

but the modeled north directed component is larger than the measured u_y.

7. Discussion

[34] Our model calculations have shown that the present-day stress and velocity field of the Alpine-Pannonian region can be described reasonably well with a thin sheet model, a Newtonian viscous rheology and a low rheology contrast between the Adriatic and the European plates below about $\eta < 3$. This result is interesting, because viscous flow of most rocks is characterized by high power law exponents. In order to remain undeformed, the European foreland must be at least 10 times as hard as the Eastern Alps and the Pannonian basin is characterized by about 80% of the viscosity of the Eastern Alps, with higher or lower viscosity contrasts resulting horizontal velocities that are too small. These results were obtained using boundary conditions that match the Euler pole of *Nocquet and Calais* [2003].

[35] As viscous and elastic constitutive relationships correspond for incremental calculations ($t = 0$) our results can directly be compared to results of elastic models. For example, *Bada et al.* [1998] showed that with an elastic model the stress field in the Pannonian basin can be best reproduced if convergent boundary conditions are applied not only along the Dinaric front, but also along the edge of the Bohemian massif and in the Southern Carpathians. Small differences between the modeled stress field shown in Figure 6 and the results of *Bada et al.* [1998] are due to these different boundary constraints. Also, in contrast to our study, *Bada et al.* [1998] used the Euler pole of *Ward* [1994], which is located some 240 km further west and 80 km further south, compared to the Euler pole of *Nocquet and Calais* [2003] used here. Similar to our study, *Bada et al.* [1998] showed that the orientation of the stress field is only dependent on the boundary conditions and that internal rheology variations in the model region have little influence on the orientation of σ_H.

[36] Mismatches between the modeled and measured velocity field are strongly dependent on internal rheological variations. GPS time series are still short and measured residual velocities are typically associated with large error

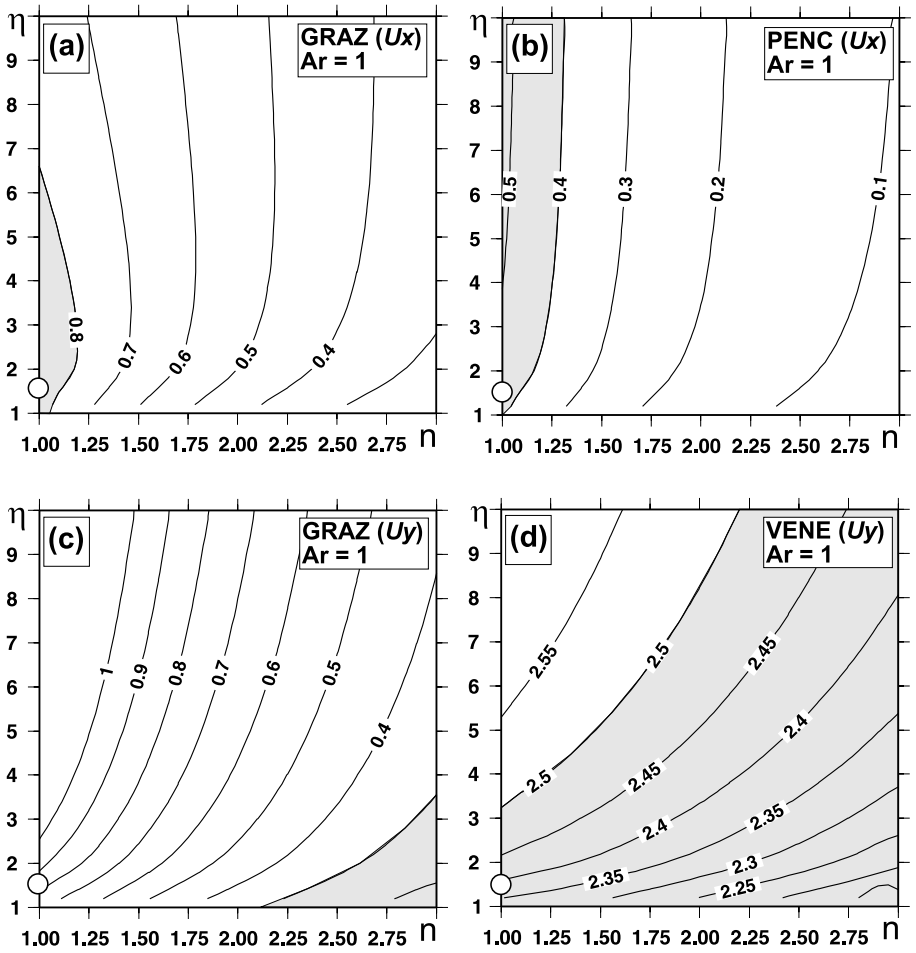

Figure 8. Contour plots for modeled north and east directed components of velocity (u_x and u_y) at selected GPS stations in mm yr^{-1}. Each plot contains 100 model runs ranging from $\eta = 1$ to $\eta = 10$ and $n = 1$ to $n = 3$. All plots are calculated for $Ar = 1$. Shaded areas show the measured velocity within errors after *Nocquet and Calais* [2003]. See Figures 1b and 5 for location of selected GPS sites. From Figure 1b it may be seen that VENE shows only small u_x and PENC shows no u_y. Plots for these velocities are therefore not shown. The white dot shows n and η used in Figures 9–11 and matches measured velocities at all considered stations best.

bars. For example, the GPS sites MOPI, BZRG and UNPG (Figure 2c) show standard deviations in the same order of magnitude as the residual velocities themselves, so that they cannot be used for the comparison with the modeled results. Other GPS stations show erratic trends such as an annual cyclicity of elevation changes (e.g., HFLK). The motion of crustal blocks, especially in the upper crust may be significantly influenced by large strike-slip faults that we have not considered in our thin sheet model. Crustal blocks move along these (preexisting) faults zones and remain internally undeformed. Fault zones may not be oriented optimally relative to the present-day stress field. We interpret that the deviation of the northward velocity at GRAZ from our modeled is caused by active faulting, as indicated by recent seismicity in the region. The permanent GPS station GRAZ is situated at the point of maximal change of the orientation of crustal motion: within 100 km west-east distance, the velocity field rotates from north-south to east-west. For that reason this point is extremely sensitive to small changes in the boundary conditions, the collision geometry or discontinuities like faults.

7.1. Changes Over Time

[37] This study has shown that the present-day tectonics of the Adriatic-European collision zone can be described with an indenter that is only 1.5 times as viscous as the Eastern Alps, using incremental model calculations. These results suggest that a region of high surface topography will develop in the Adriatic-Dinaric junction zone (Figure 9c). While we are not in a position to test this prediction for the future, it is clear that the current region of highest topography is not in this region, but inside the Eastern Alps. This suggests that the rheology used to reproduce the present-day velocity and strain rate fields in Figure 9, is unlikely to be

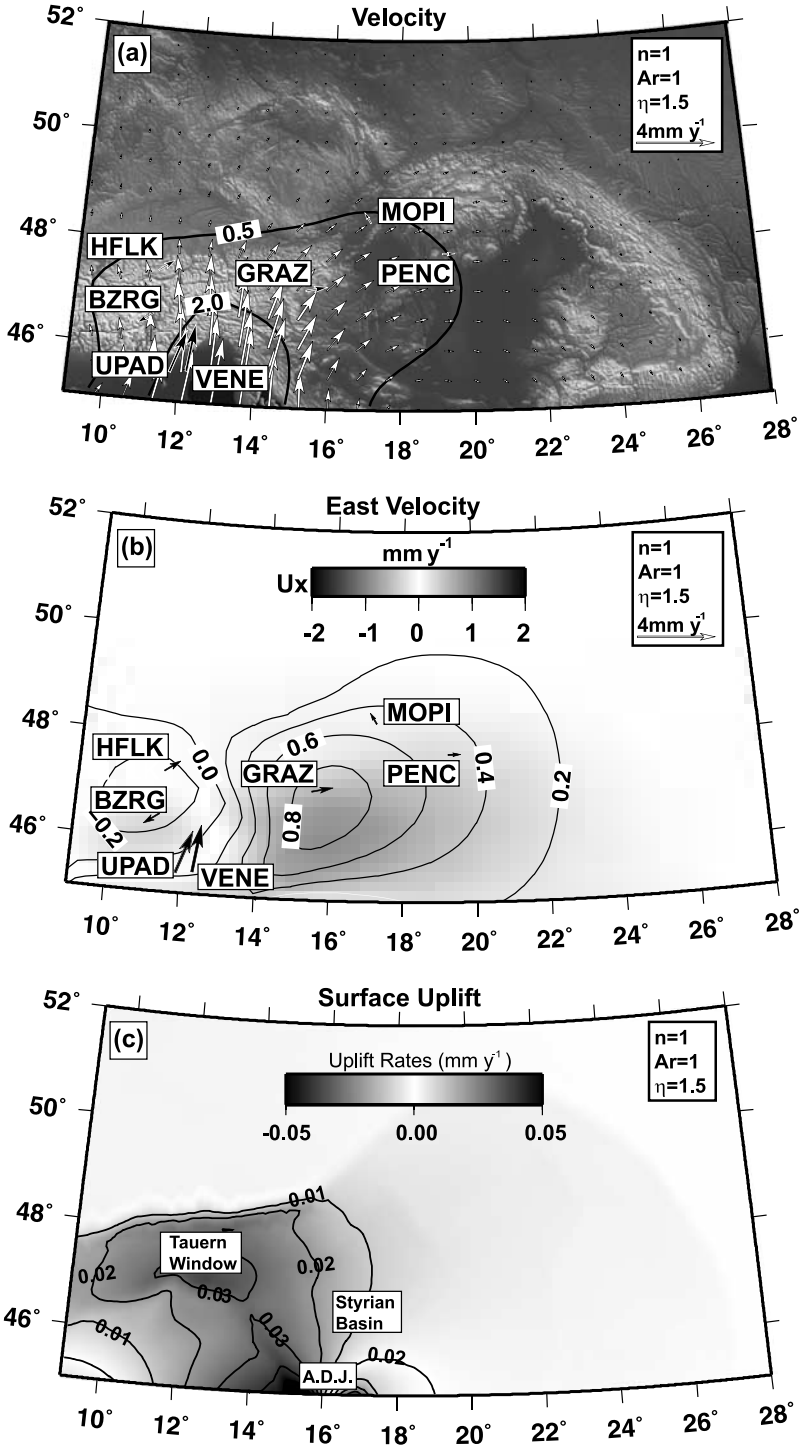

Figure 9. Modeled velocities and uplift rates using the best fit estimates from Figure 8 with $n = 1$ and $\eta = 1.5$. (a) Comparison of modeled (white arrows) and measured (black arrows) horizontal velocities. Measured velocities are relative to the central Europe reference frame after *Nocquet and Calais* [2003] and are also shown in Figure 9b. GPS stations are labeled using the internationally used abbreviations. The two contours shown are for the modeled velocity field and are labeled in mm yr^{-1}. (b) Contour plot for east-west directed components of the velocity field. Maximum velocities are shaded, while zero velocity is unshaded. The contours are for u_x in mm yr^{-1}. (c) Modeled surface uplift rate for the same parameters as in Figure 9b in mm yr^{-1} as calculated from the vertical strain rate. A.D.J. refers to the Adriatic-Dinaric junction zone. Note that these modeled uplift rates are significantly lower than those observed.

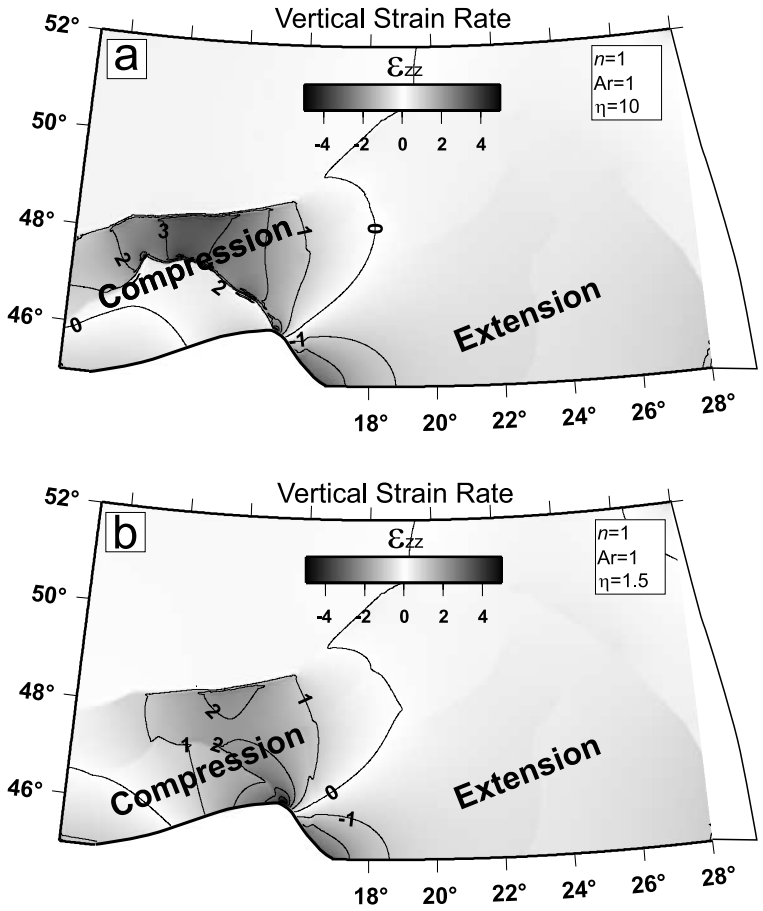

Figure 10. Time-dependent model of the collision between the Adriatic and European plates. Contour plots show vertical strain rate after 30 m.y. of convergence. Contours are multiples of 10^{-16} s^{-1}. Boundary conditions are slightly changed from Figures 6–9 to simulate the tectonic setting in the Miocene better, but the convergence rate between the Adriatic and European plates was left unchanged from Figures 6–9. Changes include tension along the eastern boundary, slip along the southern boundary, and no topography at time zero. (a) Viscosity of the indenter at 10 times the viscosity of the Eastern Alps. (b) Viscosity of the indenter at 1.5 times the viscosity of the Eastern Alps. The contour for zero vertical strain rate separates regions of compression from regions of extension. Note that for realistic convergence rates, no extension occurs within the Eastern Alps in either Figure 10a or Figure 10b despite a significant pull in the east.

the same as that at the onset of the collision. In order to test our speculation that the rheology contrast between Adriatic plate and Eastern Alps has decreased over time, we have performed a series of time-dependent calculations that describe the evolution of the region over the last 30 m.y. (Figure 10). In contrast to Figures 6–9, the model runs shown in Figure 10 were started without topography using a flat thin sheet model. Also, in order to reflect the Miocene tectonic setting better, a pull was exerted along the eastern boundary and, in absence of better geological constraints, a free-slip boundary condition was applied to the eastern half of the southern margin to reduce the boundary effects. While we will proceed in this discussion to use these somewhat loosely justified boundary conditions, we emphasize that our model has some significant shortcomings for time dependent considerations. In particular, the model does not consider faults or erosion, which both are an integral part of the Miocene evolution of the orogen.

[38] Figure 10 shows that the bulk of crustal thickening over time occurs within the orogenic wedge of the Eastern Alps only if the indenter is at least 10 times as viscous as the Eastern Alps (Figure 10a). In contrast, the geometry of the orogen develops in a much more distributed way, if the indenter is characterized by $\eta = 1.5$ throughout its evolution (Figure 10b). Since it is observed that (1) the crustal thickness inside the Eastern Alps is significantly higher than in the Adriatic plate and (2) the Miocene extrusion was largely confined to the orogenic wedge, it is argued that the Adriatic indenter must have been significantly more viscous in the Miocene than today (at least 10 times as viscous as

the Eastern Alps). These observations also indicate that the triangular shape of the indenter is already a Miocene feature, because other indenter shapes result in very differently distributed deformations. *Robl and Stüwe* [2005] have shown that progressive deformation will flatten initially triangular shaped indenters unless the viscosity contrast to the foreland is at least 10. This is in some contrast to *Frisch et al.* [1998] who argued that the Adriatic indenter was originally rectangular in shape and evolved into a triangular shape by the activation of the Guidicarie fault. In contrast, *Viola et al.* [2001] showed that the Periadriatic fault has never been a straight and that the Guidicarie fault was already part of the Periadriactic fault system, which implies a primarily triangular shaped indenter.

[39] The result of Figure 10 has a number of predictions for the tectonic evolution of the region over the last 30 m.y. First, the vertical strain rates predicted by Figure 10 (using convergence velocities from the present day) are far too small to build up an orogen. Modeled crustal thickening rates do not exceed a few tens of millimeters per year which is not even enough to compensate erosion (Figures 9c and 10). For that reason it is likely that the convergence rate was larger in the past and decreased with the absence of the slab-pull force after the slab break off [*von Blanckenburg and Davies*, 1995], although parts of the subducted European plate still appear attached [*Lippitsch et al.*, 2003]. As shown by *Houseman and England* [1993], significant crustal thickening and topography build up occur within a realistic time span only at convergence rates of about 50 mm yr^{-1}.

[40] Second, the results presented above allow inferences about the middle Miocene large-scale orogen-parallel extension. Large scale extensional features like the Brenner or Katschberg fault cannot exclusively be explained by tensional forces caused by the rollback of the subduction zone beneath the Carpathian arc in the east (assuming a plate retreat of 50 mm yr^{-1}). Even at the low present-day north-south convergence velocities of around 4 mm yr^{-1}, the roll back of the subduction zone in the east is not sufficient to cause extension within the Eastern Alps (Figures 10a and 10b). Two alternatives present themselves. (1) *Selverstone* [1988] has argued that the Miocene extension in the Tauern Window is related to dextral displacement along the Periadriatic fault. As the results discussed here assume the model region as a fault-free continuum, this idea remains untested but provides an interesting possibility for further modeling. (2) *Stüwe and Sandiford* [1995] suggested that thinning of the mantle part of the lithosphere during the Miocene provided an additional input of potential energy into the Tauern region. They argued that the Miocene extension was related to this event and also suggested this as an explanation for the simultaneous metamorphic Tauern event.

[41] Third, Figure 10 can also be used to infer causes of the predicted change in rheology contrast. Changes of the rheology contrast between the Adriatic plate and the Eastern Alps may be invoked by either weakening of the Adriatic plate or by strengthening the Eastern Alps. We argue that there is good geological evidence that the Eastern Alpine orogenic wedge strengthened substantially since the Badenian-Sarmatian boundary (13 Ma). With the cessation of subduction beneath the Carpathian arc, extension stopped, the heat flow (that was substantially perturbed in the middle Miocene [e.g., *Sachsenhofer et al.*, 1997]) decreased and the lithospheric strength increased. The rheology contrast between the Adriatic indenter and the Eastern Alps became smaller. Potential energy gradients between the overthickened crust in the Eastern Alps and the Adriatic indenter led to the propagation of the main deformation into the Southern Alps, with several km of uplift within a few million years [*Zattin et al.*, 2003]. This is also indicated by the high seismicity within the Adriatic indenter. The seismically calm domain of the Eastern Alps may confirm this, as it appears to indicate that a balance between the driving force and the gravitational potential energy has been reached there. However, this region belongs to the fastest uplifting part of the orogen, so that this model for seismically calm elevations may not apply.

7.2. Gravitational Collapse Versus Lateral Expulsion

[42] The lateral extrusion of the Eastern Alps described by *Ratschbacher et al.* [1991a, 1991b] is caused by both gravitational collapse and tectonic escape. Our model allows us to place constraints on the relative importance of these two processes. Figure 11a shows the velocity field in the study region that occurs because of gravitational collapse only. This was obtained by refraining from applying velocity boundary conditions along the southern margin, so that no tectonic escape is forced. As a consequence, the velocity field shown in Figure 11a arises entirely because of potential energy variations and velocities follow gradients of crustal thickness. Accordingly, the east directed velocity field in the Eastern Alps turns southward in the Pannonian basin. Scaled to an Argand number of $Ar = 1$ (implying a viscosity of 1.36×10^{23} Pa s for the Eastern Alps) the maximum horizontal velocity due to gravity is no larger than 0.1 mm yr^{-1}. This corresponds to about 10% of the total velocity when using convergent boundary conditions (Figure 9a). Correspondingly, for an unrealistic Argand number of $Ar = 10$ (implying a viscosity of 1.36×10^{22} Pa s), maximum velocities would be around 1 mm yr^{-1} or about half of the lateral extrusion rate. These results are in some contrast to *Bada et al.* [2001] who suggested that gravitational potential energy may provide significant contributions to the stress and strain field in the Pannonian basin, but the results correspond to those of *Selverstone* [2005] who also argued that the majority of the east directed displacement of the Alps is due to tectonic escape.

[43] Gravitational collapse can be illustrated by plotting vertical strain rates (Figure 11b) or by tracking the topography through time (Figures 11c and 11d). Mountainous regions with the highest topography and the largest crustal thickness show the highest negative values for the vertical strain rate (i.e., horizontal extension), while domains covered by basins show compression (positive vertical strain rates). For $Ar = 1$, the highest negative values for the vertical strain rate occur in the Tauern Window region and are around 4×10^{-17} s^{-1}. Figures 11c and 11d illustrate that it would take about 160 m.y. to reduce the highest

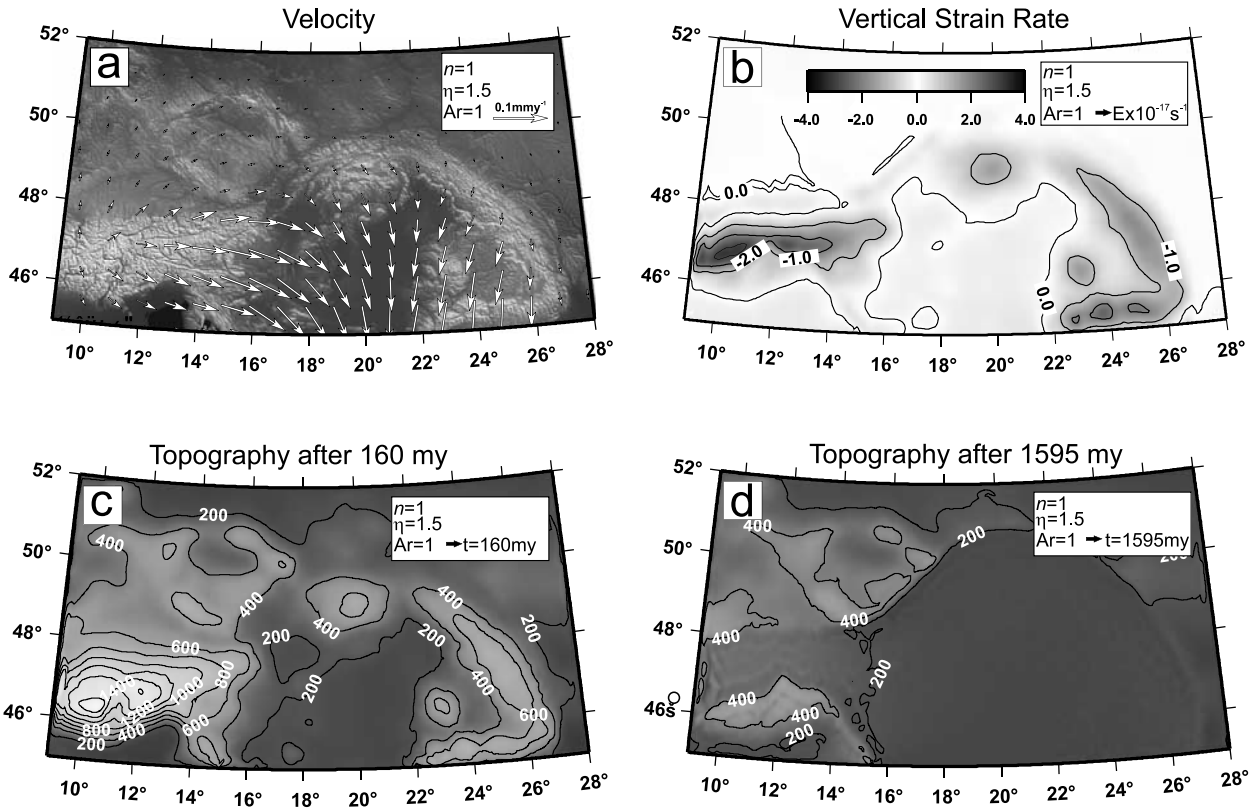

Figure 11. Plots showing the gravitational collapse if no forces are applied at the boundaries. (a) Velocity field that is exclusively due to the gravitational collapse (arrows). (b) Contours for the vertical strain rate in multiples of 10^{-17} s^{-1} for $Ar = 1$. (c and d) Decrease of elevation with elapsed time.

elevation of the Eastern Alps to about 1500 m (Figure 11c) and almost 1600 m.y. to remove the Eastern Alps by gravitational collapse, neglecting erosion (Figure 11d). These times scale linearly with Argand number: For Ar = 10, rates of vertical strain rates are 10 times as large and topography decays ten times as rapid. Nevertheless, the change from positive to negative vertical strain rate; that is, the change from a compressional to and extensional regime does not change with Argand number. In Figure 11b it may be seen that when horizontal compression is neglected the contour for zero vertical strain rate covers a region that is much larger than the aseismic zone shown in Figure 2a.

7.3. Uplift and Strain Rates

[44] Horizontal strain rates in the Eastern Alps are not very well known and an interpretation of seismic moment tensors in terms of strain rate is still missing for the Eastern Alps. We therefore refrain from interpreting horizontal strain rates but briefly discuss surface uplift rates predicted by the model, which are, in isostatic equilibrium, directly related to the vertical strain rates. However, we note that the interpretation of uplift rates from a model that does not consider erosion is difficult at best [*England and Molnar*, 1990]. Moreover, uplift rates of the Eastern Alps are both not very well known and unlikely to relate to vertical strain rate. Only time integrated ballpark estimates for uplift rates since the Miocene exist in the study region [e.g., *Frisch et al.*, 1998; *Zattin et al.*, 2003; *Dunkl et al.*, 2003] and present-day measurements [e.g., *Ruess and Höggerl*, 2002] are unlikely to be representative, as they predict subsidence in parts of the study region where there is clear geological evidence for recent uplift. In fact, the geodetically determined uplift rates for the Eastern Alps are known to be related to elastic rebound following the deglaciation, rather than the response to vertical strain rates [*Ruess and Höggerl*, 2002].

[45] Regardless, our model can be used to show that crustal thickening is only of 2nd order importance to surface uplift. Within the model uplift rates are related to vertical strain rate by $\Delta E = S\dot{\varepsilon}_{zz}/\Delta\rho$ where ΔE stand for the uplift rate, S for the crustal thickness, $\dot{\varepsilon}_{zz}$ for the vertical strain rate and $\Delta\rho$ is the density contrast. Uplift rates shown in Figure 9c are around tens of meters per million years Highest uplift rates are modeled in the Tauern Window and at the corner of the Adriatic-Dinaric junction zone (Figure 9c), which is consistent with observations: The Tauern Window is the region of highest topography in the study region and the Adriatic-Dinaric junction zone has been described as a currently rapidly uplifting region by *Zattin et al.* [2003]. In the Styrian basin, there is also a reasonable correspondence between modeled and measured uplift rates: the Styrian basin is currently about

200–300 meters above sea level and the last marine sedimentation occurred around 10 Ma, suggesting mean uplift rates around 20–30 m m.y.$^{-1}$.

8. Conclusion

[46] The stress and velocity field of the Alpine-Pannonian realm can be successfully reproduced with a two-dimensional thin viscous sheet model and boundary conditions that reflect the present-day collision geometry between the Adriatic and European plate. The orientation of the intraplate stress field is strongly dependent on these boundary conditions and is therefore used as an independent test for our assumed boundary conditions. However, the orientation of the intraplate stress field is robust toward internal rheology contrasts between different geological domains in the model region.

[47] In contrast to the orientation of the stress field, the velocity field is strongly dependent on internal rheology contrasts between different geological domains in the Alpine-Pannonian realm. We suggest that the region may be viewed in terms of four regions of different viscous rheology: the Pannonian basin, the European foreland, the Eastern Alps and the Adriatic indenter. The Pannonian basin and the European foreland are suggested to be 0.8 and 10 times as viscous as the Eastern Alps, respectively. The value for the European foreland is large enough to suppress significant velocities in this region. The value for the Pannonian basin is fairly well constrained as lower as well as higher values for its viscosity contrast would both cause a decrease in the velocity field below the values observed at GPS sites in the basin.

[48] The GPS-determined velocity field in the model region can best be reproduced if the Adriatic indenter is less than 3 times as strong as the Eastern Alps and is described with a Newtonian rheology. This estimate is largely independent of the Argand number. A stronger rheology is not consistent with the extensive deformation within the Adriatic domain. The high seismicity within the Adriatic domain and the absence of seismicity in the Eastern Alps suggests that crustal deformation propagated to the proximal domains of the orogen driven by gradients in the potential energy.

[49] The overall geometry of the Eastern Alps, the shape of the Adriatic indenter, as well as the timing and distribution of crustal thickness and topography imply that the similar viscosity of Adriatic plate and Eastern Alps is a recent feature and that this contrast was significantly higher in the Miocene. We suggest that the contrast was higher because the Eastern Alps was significantly softer at this time, allowing the bulk of the shortening to be accommodated within the European plate.

[50] The lateral velocity of the Eastern Alps, which has been termed lateral extrusion, is 10% due to gravitational collapse and 90% due to lateral escape. This ratio is for an Argand number of the orogen of 1. For this Argand number, the viscosity of the Eastern Alps scales to about 10^{23} Pa s and the gravitational collapse alone would take more than 1000 m.y. to destroy the topography. In the Miocene the viscosity would have been around 10^{22} Pa s. These values scale linearly with the Argand number.

Appendix A: Scaling of Nondimensional Values

[51] Although most parameters in this paper are presented in terms of scaled values, BASIL performs calculations using dimensionless variables. Table 1 summarizes the dimensionless variables and shows how to scale them to actual values. Of the first three lines, (length, velocity and time) only two are independent and the third is given by the other two. When using spherical coordinates, the length scaling is hard wired through D and the velocity dimension is typically given by the scale for the boundary conditions (e.g., $u' = 1$ corresponds to $U_0 = 4$ mm yr^{-1}) so that dimensionless time is readily converted to real time from the other two variables (i.e., $t' = 1$ corresponds to $t = 1594.5$ m.y. or $\dot{\varepsilon}' = 1$ corresponds to $\dot{\varepsilon} = 1.99 \times 10^{-17}$ s^{-1}). Similarly, of the last two lines (stress and viscosity) only one is independent (and its dimension can be freely chosen) and the other one is then implicitly determined, because the viscous constitutive relationship states that stress is directly related to viscosity via strain rate. However, when using the Argand number Ar as an input variable, then neither stress nor viscosity are independent. For Newtonian rheologies, where stress is linearly related to strain rate, viscosity is related to Ar by $\eta = g L^2 \rho_c (1 - \rho_c/\rho_m)/(2\ Ar\ U_0)$, where the factor 2 arises from the relationship of stress to strain rate and has been mistakenly omitted by *Tenczer et al.* [2001] or *Biermeier et al.* [2001] (see also *Robl and Stüwe* [2005] for details on Argand number). Inserting the numbers for the physical parameters from above, the viscosity is $\eta = 1.36 \times 10^{23}$ Pa s for $Ar = 1$ and a dimensionless stress of $\sigma' = 1$ corresponds to $\sigma = 2.7 \times 10^6$ Pa.

Appendix B: Defining Regions Using TraceIt

[52] Within the finite element code BASIL, the triangulation process is controlled by poly files, that are used to define the model region, the shape and position of regions of variable rheology and the resolution. The tool TraceIt was coded to speed up the time consuming process of writing poly files for regions of arbitrary shape by an easy to use graphical user interface. Graphic files in jpg or bmp format can be used to trace the desired structures with a few mouse clicks. An outline function allows to generate a regular outline with a user defined width around a traced feature. A trap function enables to meet exactly a previous defined point. Two text fields allow to define points manually. A function to create a circle or an ellipse is also implemented. The defined regions are itemized in a list box. Defined regions can be streamed to and from disk, so that once defined regions can be stored for further projects. TraceIt can also write the defined regions as GMT readable multisegment files. TraceIt was written to trace geological maps and to match the input for the finite element code BASIL, but can be a useful tool for a wide range of modeling software that require real geometries from maps or

rocks, for example when tracing microstructures as input for grain boundary codes. TraceIt is free software and can be obtained from the first author.

[53] **Acknowledgments.** Lynn Evans is thanked for her help with implementing the topography interpolation into the finite element code BASIL and her patient help with a countless number of questions. G. Houseman is thanked for the spherical thin viscous sheet model and for his continuous support and interest in this project. T. Barr is thanked for his help with understanding the scaling of nonlinear rheologies. F. Neubauer and N. Mancktelow are thanked for their extremely constructive careful reviews and O. Oncken for his efficient editorial handling. H. Sünkel and P. Pesec are thanked for discussions of the geodetics of the study region and for warning us of the tectonic relevance of the GPS time series from station HFLK. The project was supported by FWF project P-15474.

References

Anderson, H. A., and J. A. Jackson (1987), Active tectonics of the Adriatic region, *Geophys. J. R. Astron. Soc.*, *91*, 937–983.

Bada, G., S. Cloetingh, P. Gerner, and F. Horváth (1998), Sources of recent tectonic stress in the Pannonian region: Inferences from finite element modeling, *Geophys. J. Int.*, *134*, 87–101.

Bada, G., F. Horváth, P. Gerner, and I. Fejes (1999), Review of the present-day geodynamics of the Pannonian basin: Progress and problems, *J. Geodyn.*, *27*, 501–527.

Bada, G., F. Horvath, S. Cloetingh, and D. Coblentz (2001), Role of topography-induced gravitational stresses in basin inversion: The case study of the Pannonian basin, *Tectonics*, *20*, 343–363.

Barr, T. D., and G. A. Houseman (1996), Deformation fields around a fault embedded in a non-linear ductile medium, *Geophys. J. Int.*, *125*, 473–490.

Behrmann, J. H. (1988), Crustal-scale extension in a convergent orogen: The Sterzing-Steinach mylonite zone in the Eastern Alps, *Geodin. Acta*, *2*, 63–73.

Biermeier, C., K. Stüwe, and T. D. Barr (2001), The rotation rate of cylindrical objects during simple shear, *J. Struct. Geol.*, *23*, 765–776.

Castellarin, A., and L. Cantelli (2000), Neo-Alpine evolution of the southern Eastern Alps, *J. Geodyn.*, *30*, 251–274.

Cloetingh, S., and A. Lankreijer (2001), Lithospheric memory and stress field controls on polyphase deformation of the Pannonian basin–Carpathian system, *Mar. Pet. Geol.*, *18*, 3–11.

Dewey, J. F. (1988), Extensional collapse of orogens, *Tectonics*, *7*, 1123–1139.

Dunkl, I., and A. Demény (1997), Exhumation of the Rechnitz Window at the border of the Eastern Alps and Pannonian basin during Neogene extension, *Tectonophysics*, *272*, 197–211.

Dunkl, I., B. Grasemann, and W. Frisch (1998), Thermal effects of exhumation of a metamorphic core complex on hanging wall syn-rift sediments: An example from the Rechnitz Window, Eastern Alps, *Tectonophysics*, *297*, 31–50.

Dunkl, I., W. Frisch, and G. Grundmann (2003), Zircon fission track thermochronology of the southeastern part of the Tauern Window and the adjacent Austroalpine margin, Eastern Alps, *Eclogae Geol. Helv.*, *96*, 209–217.

England, P. C., and G. A. Houseman (1986), Finite strain calculations of the continental deformation: 2. Comparison with the India-Asia collision zone, *J. Geophys. Res.*, *91*, 3664–3676.

England, P. C., and G. A. Houseman (1989), Extension during continental convergence, with application to the Tibetan Plateau, *J. Geophys. Res.*, *96*, 17,561–17,579.

England, P. C., and P. Molnar (1990), Surface uplift, uplift of rocks and exhumation of rocks, *Geology*, *18*, 1173–1177.

Farr, T. G., and M. Kobrick (2000), Shuttle Radar Topography Mission produces a wealth of data, *Eos Trans. AGU*, *81*, 583, 585.

Frisch, W., J. Kuhlemann, I. Dunkl, and A. Brügel (1998), Palinspastic reconstruction and topographic evolution of the Eastern Alps during late Tertiary tectonic extrusion, *Tectonophysics*, *297*, 1–15.

Frisch, W., I. Dunkl, and J. Kuhlemann (2000), Post-collisional large-scale extension in the Eastern Alps, *Tectonophysics*, *327*, 239–265.

Fügenschuh, B., D. Seward, and N. Mancktelow (1997), Exhumation in a convergent orogen: The western Tauern Window, *Terra Nova*, *9*, 213–217.

Genser, J., and F. Neubauer (1989), Low angle normal faults at the eastern margin of the Tauern Window (Eastern Alps), *Mitt. Oesterr. Geol. Ges.*, *81*, 233–243.

Genser, J., J. D. van Wees, S. Cloetingh, and F. Neubauer (1996), Eastern Alpine tectono-metamorphic evolution: Constraints from two-dimensional *P-T-t* modeling, *Tectonics*, *15*, 584–604.

Gölke, M., and D. Coblentz (1996), Origin of the European regional stress field, *Tectonophysics*, *266*, 11–24.

Grenerczy, G., A. Kenyeres, and I. Fejes (2000), Present crustal movement and strain distribution in central Europe inferred from GPS measurements, *J. Geophys. Res.*, *105*, 21,835–21,846.

Hansen, K. M., and V. S. Mount (1990), Smoothing and extrapolation of crustal stress orientation measurements, *J. Geophys. Res.*, *95*, 1155–1165.

Horváth, F., and S. Cloetingh (1996), Stress-induced late-stage subsidence anomalies in the Pannonian basin, *Tectonophysics*, *266*, 287–300.

Houseman, G. A., and P. C. England (1986), Finite strain calculations of continental deformation: 1. Method and general results for convergent zones, *J. Geophys. Res.*, *91*, 3651–3663.

Houseman, G. A., and P. C. England (1993), Crustal thickening versus lateral expulsion in the India-Asian continental collision, *J. Geophys. Res.*, *98*, 12,233–12,249.

Kuhlemann, J., and O. Kempf (2002), Post-Eocene evolution of the North Alpine foreland basin and its response to Alpine tectonics, *Sediment. Geol.*, *152*, 45–78.

Kuhlemann, J., W. Frisch, I. Dunkl, and B. Székely (2001), Quantifying tectonic versus erosive denudation by the sediment budget: The Miocene core complexes of the Alps, *Tectonophysics*, *330*, 1–23.

Lippitsch, R., E. Kissling, and J. Ansorge (2003), Upper mantle structure beneath the Alpine orogen from high-resolution teleseismic tomography, *J. Geophys. Res.*, *108*(B8), 2376, doi:10.1029/2002JB002016.

Liu, Y., J. Genser, R. Handler, G. Friedl, and F. Neubauer (2001), $^{40}Ar/^{39}Ar$ muscovite ages from the Penninic-Austroalpine plate boundary, Eastern Alps, *Tectonics*, *20*, 526–547.

Mancktelow, N. S., D. F. Stöckli, B. Grollimund, W. Müller, B. Fügenschuh, G. Viola, and D. Seward (2001), The DAV and Periadriatic fault systems in the Eastern Alps south of the Tauern Window, *Int. J. Earth Sci.*, *90*, 593–622.

Molnar, P., and H. Lyon-Caen (1988), Some simple physical aspects of the support, structure, and evolution of mountain belts, in *Processes in Continental Lithospheric Deformation*, edited by S. P. Clark Jr., B. C. Burchfiel, and J. Suppe, *Geol. Soc. Am. Spec. Pap.*, *218*, 179–207.

Nemes, F., F. Neubauer, S. Cloetingh, and J. Genser (1997), The Klagenfurt basin in the Eastern Alps: An intra-orogenic decoupled flexural basin?, *Tectonophysics*, *282*, 189–203.

Neubauer, F., J. Genser, W. Kurz, and X. Wang (1999), Exhumation of the Tauern Window, Eastern Alps, *Phys. Chem. Earth, Part A*, *24*, 675–680.

Nocquet, J.-M., and E. Calais (2003), Crustal velocity field of western Europe from permanent GPS array solutions, 1996–2001, *Geophys. J. Int.*, *154*, 72–88.

Peresson, H., and K. Decker (1997), The Tertiary dynamics of the northern Eastern Alps (Austria): Changing palaeostresses in a collisional plate boundary, *Tectonophysics*, *272*, 125–157.

Pfiffner, O. A., S. Ellis, and C. Beaumont (2000), Collision tectonics in the Swiss Alps: Insight from geodynamic modeling, *Tectonics*, *19*, 1065–1094.

Ratschbacher, L., W. Frisch, F. Neubauer, S. M. Schmid, and J. Neugebauer (1989), Extension in compressional orogenic belts: The Eastern Alps, *Geology*, *17*, 404–407.

Ratschbacher, L., W. Frisch, H. G. Linzer, and O. Merle (1991a), Lateral extrusion in the Eastern Alps: 2. Structural analysis, *Tectonics*, *10*, 257–271.

Ratschbacher, L., O. Merle, P. Davy, and P. Cobbold (1991b), Lateral extrusion in the Eastern Alps: 1. Boundary conditions and experiments scaled for gravity, *Tectonics*, *10*, 245–256.

Reinecker, J., and W. A. Lenhardt (1999), Present-day stress field and deformation in eastern Austria, *Int. J. Earth Sci.*, *88*, 532–550.

Robl, J., and K. Stüwe (2005), Continental collision with finite indenter strength: 1. Concept and model formulation, *Tectonics*, *24*, TC4005, doi:10.1029/2004TC001727.

Rosenberg, C. L. (2004), Shear zones and magma ascent: A model based on a review of the Tertiary magmatism in the Alps, *Tectonics*, *23*, TC3002, doi:10.1029/2003TC001526.

Royden, L., F. Horváth, A. Nagymarosy, and L. Stegena (1983), Evolution of the Pannonian basin system: 2. Subsidence and thermal history, *Tectonics*, *2*, 91–137.

Ruess, D., and N. Höggerl (2002), Bestimmung rezenter Höhen- und Schwereänderungen in Österreich (abstract), in *PANGEO AUSTRIA*, edited by G. Friedl et al., p. 151, Inst. für Geol. und Paläontol., Univ. Salzburg, Salzburg, Austria.

Sachsenhofer, R. F. (2001), Syn- and post-collisional heat flow in the Cenozoic Eastern Alps, *Int. J. Earth Sci.*, *90*, 579–592.

Sachsenhofer, R. F., A. Lankreijer, S. Cloetingh, and F. Ebner (1997), Subsidence analysis and quantitative basin modeling in the Styrian basin (Pannonian basin system, Austria), *Tectonophysics*, *272*, 175–196.

Scarascia, S., and R. Cassinis (1997), Crustal structures in the central-eastern Alpine sector: A revision of available DSS data, *Tectonophysics*, *271*, 157–188.

Schmid, S. M., A. Zingg, and M. Handy (1987), The kinematics of movements along the Insubric Line and the emplacement of the Ivrea zone, *Tectonophysics*, *135*, 47–66.

Schmid, S. M., H. R. Aebli, F. Heller, and A. Zingg (1989), The role of the Periadriatic Line in the tectonic evolution of the Alps, in *Conference on Al-*

pine Tectonics, edited by M. P. Coward, D. Dietrich, and R. G. Park, *Geol. Soc. London Spec. Publ.*, *45*, 153–171.

Selverstone, J. (1988), Evidence for east-west crustal extension in the Eastern Alps: Implication for the unroofing history of the Tauern Window, *Tectonics*, *7*, 87–105.

Selverstone, J. (2005), Are the Alps collapsing?, *Annu. Rev. Earth Planet. Sci.*, *33*, 113–132.

Shewchuck, J. R. (2002), Delaunay refinement algorithms for triangular mesh generation, *Comput. Geometry Theory Appl.*, *22*, 21–74.

Sonder, L. J., and P. England (1986), Vertical averages of rheology of the continental lithosphere: Relation to "thin sheet" parameters, *Earth Planet. Sci. Lett.*, *77*, 81–90.

Stüwe, K., and T. D. Barr (2000), On the relationship between surface uplift and gravitational extension, *Tectonics*, *19*, 1056–1064.

Stüwe, K., and M. Sandiford (1995), Mantle-lithospheric deformation and crustal metamorphism with some speculations on the thermal and mechanical significance of the Tauern event, Eastern Alps, *Tectonophysics*, *242*, 115–132.

Tapponnier, P., G. Peltzer, A. Y. Le Dain, R. Armijo, and P. Cobbold (1982), Propagating extrusion tectonics in Asia: New insights from simple experiments with plasticine, *Geology*, *10*, 611–616.

Tenczer, V., K. Stüwe, and T. D. Barr (2001), Pressure anomalies around cylindrical objects in simple shear, *J. Struct. Geol.*, *23*, 777–788.

Viola, G., N. S. Mancktelow, and D. Seward (2001), Late Oligocene-Neogen evolution of Europe-Adria collision: New structural and geochronological evidence from the Guidicarie fault system (Italian Eastern Alps), *Tectonics*, *20*, 999–1020.

von Blanckenburg, F., and J. H. Davies (1995), Slab breakoff: A model for syncollisional magmatism and tectonics in the Alps, *Tectonics*, *14*, 120–131.

Ward, S. N. (1994), Constraints on the seismotectonics of the central Mediterranean from very long baseline interferometry, *Geophys. J. Int.*, *117*, 441–452.

Wessel, P., and W. H. F. Smith (1991), Free software helps map and display data, *Eos Trans. AGU*, *72*, 441–446.

Westaway, R. (1990), The Tripoli, Libya, earthquake of September 4, 1974: Implications for active tectonics of the central Mediterranean, *Tectonics*, *9*, 231–248.

Willingshofer, E., and S. Cloetingh (2003), Present-day lithospheric strength of the Eastern Alps and its relationship to neotectonics, *Tectonics*, *22*(6), 1075, doi:10.1029/2002TC001463.

Willingshofer, E., J. D. van Wees, S. Cloetingh, and F. Neubauer (1999), Thermomechanical consequences of Cretaceous continent-continent collision in the eastern Alps (Austria): Insights from two-dimensional modeling, *Tectonics*, *18*, 809–826.

Zattin, M., C. Stefani, and S. Martin (2003), Detrital fission-track analysis and sedimentary petrofacies as key of Alpine exhumation: The example of the Venetian foreland (European Southern Alps, Italy), *J. Sediment. Res.*, *73*, 1051–1061.

J. Robl and K. Stüwe, Institut für Erdwissenschaften, Universität Graz, Heinrichstr. 26, A-8010 Graz, Austria. (joerg.robl@uni-graz.at)